ABSTRACT

DEVELOPMENT OF A PYTHON BASED EMITTANCE CALCULATOR AT FERMILAB SCIENCE & TECHNOLOGY (FAST) FACILITY

A. T. Green, M.S.
Department of Physics
Northern Illinois University, 2016
Dr. Young-Min Shin, Director

Beam emittance is an important characteristic describing charged particle beams. In linear accelerators (linac), it is critical to characterize the beam phase space parameters and, in particular, to precisely measure transverse beam emittance. The quadrupole scan (quad-scan) is a well-established technique used to characterize transverse beam parameters in four-dimensional phase space, including beam emittance. A computational algorithm with PYTHON scripts has been developed to estimate beam parameters, in particular beam emittance, using the quad-scan technique in the electron linac at the Fermilab Accelerator Science and Technology (FAST) facility. This script has been implemented in conjunction with an automated quad-scan tool (also written in PYTHON) and has decreased the time it takes to perform a single quad-scan from an hour to a few minutes. From the experimental data, the emittance calculator quickly delivers several results including: geometrical and normalized transverse emittance, Courant-Snyder parameters, and plots of the beam size versus quadrupole field strength, among others. This paper will discuss the details of the techniques used, the results from several quad-scans preformed at FAST during the electron injector commissioning, and the PYTHON code used to obtain the results.

NORTHERN ILLINOIS UNIVERSITY
DE KALB, ILLINOIS

AUGUST 2016

DEVELOPMENT OF A PYTHON BASED EMITTANCE CALCULATOR AT FERMILAB SCIENCE & TECHNOLOGY (FAST) FACILITY

BY

A. T. GREEN

A DISSERTATION SUBMITTED TO THE GRADUATE SCHOOL

IN PARTIAL FULFILLMENT OF THE REQUIREMENTS

FOR THE DEGREE

MASTERS OF BASIC PHYSICS

DEPARTMENT OF PHYSICS

Dissertation Director:
Dr. Young-Min Shin

ACKNOWLEDGEMENTS

I would like to thank the following members of the FAST/NIU group for guidance and technical support as well as for the opportunity to be a part of the group and for beam time to perform these experiments:

D. Broemmelsiek, K. Carlson, D. Crawford, D. Edstrom, A. Halavanau, J. Hyun, A. Lumpkin, D. Mihalcea, P. Piot, A. Romanov, J. Ruan, J. Santucci, G. Stancari, Y.M. Shin, C. Thangaraj, and A. Valishev

TABLE OF CONTENTS

LIST OF TABLES

LIST OF FIGURES

Figure Page

CHAPTER 1

FAST FACILITY - EMITTANCE CHARACTERIZATION

1.1 Introduction

Emittance is an intrinsic quantity of charged particle beams in particle accelerators. It needs to be fully characterized in order to assure that the beamline is operational. This chapter will describe the motivation for the measurement of beam emittance and associated beam parameters, including the objectives of the work. The chapter also includes a brief introduction of the Fermilab Science and Technology (FAST) facility currently being commissioned at Fermilab.

1.2 A Need for Emittance Measurements

Emittance is a beam parameter quantifying the volume of six-dimensional phase space (x, p_x) occupied by the dynamically moving particles in a beam. In practical terms, the emittance also relates to the smallest achievable spot size and divergence:

$$\sigma = \sqrt{\beta\epsilon_g} \propto \sqrt{\epsilon_g} \tag{1.1}$$

$$\sigma\sigma' = \epsilon \Rightarrow \sigma' = \frac{\epsilon}{\sqrt{\beta\epsilon_g}} \propto \sqrt{\epsilon_g}, \tag{1.2}$$

where σ is the beam size, σ' is the divergence, β is a Courant-Snyder parameter, and ϵ_g is the geometrical emittance (further discussion of these parameters can be found in Chapter 2 [1].

There are several ways to measure emittance and one of the most common and well known methods is the quadrupole scan technique (quad-scan). Quadrupole magnets are used in modern accelerators to either focus or defocus the beam. A beam is comprised of particles with the same charge and they tend to repel each other due to space charge, the Coulomb repulsive force due to like charges. Since beams must travel through beam pipes and various structures within the accelerator, it is crucial that the beam stays focused to within the specifications of the accelerator.

In order to perform a quad-scan, the magnetic field strength of a single quadrupole magnet needs to be optimized and then the beam size is to be recorded as it changes due to the focusing/defocusing effects on an imaging screen. This simple technique is well understood, which properly fits for emittance measurements.

The quadrupole magnet field strength and beam size measurements, along with the precise knowledge of the accelerator configuration, are all that are needed to calculate the beam emittance. Emittance is a conserved quantity and as such, calculating the emittance at one location along the beamline will describe the emittance anywhere along the accelerator. Details on quad-scans and emittance calculations are described in Chapter 3.

1.3 Objective

At the FAST facility, quad-scans can take up to an hour each: the quadrupole current must be manually scanned (by knobbing the current) and for each current setting the current and beam size must be recording. For this reason, an "automated" quad-scan tool was

written in PYTHON, which shortened the time it took to perform a quad-scan to as little as 5 min [2].

However, there also existed a need for a way to quickly calculate the emittance and associated beam parameters. The goal of this project was to then develop an "emittance calculator" via PYTHON to complement the quad-scan tool. Details of these tools can be found in Chapter 6.

1.4 Fermilab Science & Technology (FAST)

It is at the FAST facility at Fermilab where the automated quad-scan and emittance calculator have been employed. FAST is an advanced superconducting radio frequency (SRF) accelerator laboratory currently under construction at Fermilab. The goal of this facility is to provide cutting edge RD and infrastructure critical to the research and development of both current and future accelerators. The main components of the FAST beamline are depicted in Fig. 1.1 (from left-to-right):

- Low-energy beamline (red) - radio-frequency gun, bucking solenoid, main solenoid, and two superconducting booster cavities (CC-1 and CC-2) capable of accelerating electrons up to 50 MeV.
- CM2 (light blue) - Cryomudule 2, an ILC-type cryomodule, for accelerating electrons up to 300 MeV.
- RFQ (dark blue) - Radio frequency quad capable of accelerating protons up to 2.7MeV.
- IOTA (blue ring) - Integrable Optics Test Accelerator proton/electron storage ring for 150 MeV electron-based experiments and 2.5 MeV proton-based experiments.

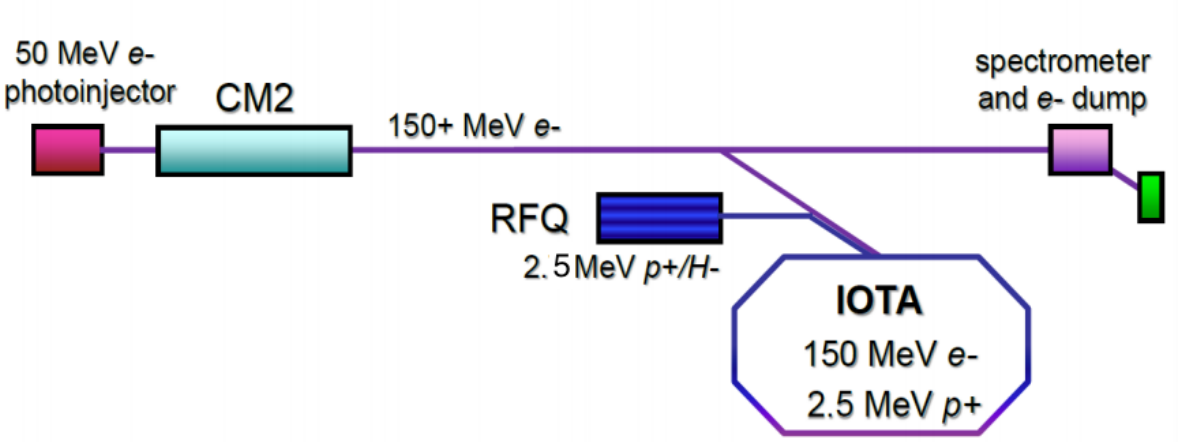

Figure 1.1: A cartoon of the FAST beamline showing the major components of the low-energy and high-energy beamlines as well as the proton injector (RFQ) and IOTA ring [3].

FAST is currently in the commissioning phase of the 50 MeV low-energy beamline, with the high-energy beamline, RFQ, and IOTA ring still under construction. The facility will soon enable a broad range of beam-based experiments to the high-energy physics community in the U.S. and abroad. The quad-scans performed in this project were performed at the low-energy beamline. Details of the components used in the quad-scan experiments will follow in the next few chapters. Several unique features of this facility include [3]:

- High repetition-rate of the electron bunches for high average power output. Linacs generally operate in a repetitive, pulsed mode.
- One of the highest peak and average brightness within the U.S. (brightness being the maximum value of the flux per unit area per unit solid angle) [6].
- An extremely stable beam.
- The advancement of superconducting radio-frequency (SRF) accelerator technology.
- A storage ring capable of supporting a broad range of ring-based advanced beam dynamics experiments.

Table 1.1 shows some of the proposed range of FAST parameters for the electron injector as compared to the International Linear Collider (ILC) nominal parameters [7]. One of the driving concepts behind the construction of this facility is that while FAST will meet or exceed several beam parameters that have been met by the accelerator community already, there are no accelerators that can currently achieve these parameters within the same facility. More details about the FAST facility can be found in [3] - [5].

Table 1.1: Proposed parameters for the FAST electron injector [3].

Parameter	**ILC nominal**	**FAST Range**
Bunch charge	$3.2\,nC$	$100\,pC\ to > 20\,nC$
Bunch spacing	$333\,ns$	$<\ 10\,ns\ to\ 10\,ns$
Bunch train	$1\,ms$	$1\,bunch\ to\ 1\,ms$
Train rep. rate	$5\,Hz$	$0.1\,Hz\ to\ 5\,Hz$
Trans. emittance	$25\,mm \cdot mrad$	$1\ to\ 100\,mm \cdot mrad$
RMS bunch length	$1\,ps$	$10\,fs\ to\ 10\,ps$
Beam energy	$300\,MeV$	$50 - 300\,MeV$

1.5 Relevant Components

There were several primary components in the beamline of the FAST facility that were used in the quad-scan experiments for this project: solenoid magnets, quadrupole magnets (quad), and transverse profile monitors (TPM). A brief discussion of these components will be given in the following sections.

1.5.1 Solenoid Magnets

In the rf-gun section of the low-energy beamline there are two identical solenoid magnets aligned with reverse polarity. A bucking solenoid surrounds the cathode and is then followed by the main solenoid. The bucking solenoid is used to cancel the magnetic fringe field from the entry of the main solenoid, which can cause emittance growth from the angular momentum kick of the main solenoid field. Since the solenoids are aligned with reverse polarity, the magnetic field from the bucking solenoid cancels the the magnetic fringe field of the main solenoid in the region of cathode. The main solenoid is then used to focus the low velocity electrons from the cathode for matching into Capture Cavity 1 (CC-1), the first superconducting accelerating cavity.

Solenoids are analogous to a magnetic lens. In the entry and exit regions, the radial magnetic (fringe) field imparts an angular moment kick to the beam, while in the main "body" of the solenoid (the area within the physical structure of the magnetic lens) the magnetic field is constant along the axis of the particle trajectory, with the motion of the particles moving in a circular manner in the transverse planes.

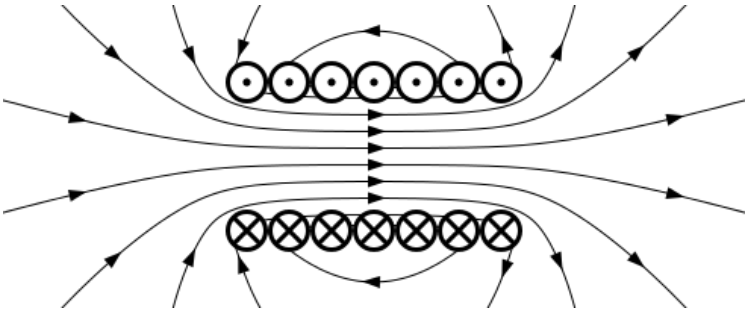

Figure 1.2: Magnetic field lines at the entrance, center, and exit of a solenoid [8].

Figure 1.2 shows the magnetic field lines for a solenoid magnet [8]. If z is the direction of the propagation of motion, with x, y being the transverse planes, then the magnetic field within the solenoid can be written as:

$$\mathbf{B_z} = \mu_0 \frac{N}{L} I, \tag{1.3}$$

where μ_0 is the permeability of free space, N is the number of turns per coil, L is the length of the solenoid, and I is the current in the wire.

The magnetic fringe field at the front and back edge of the solenoid is:

$$\mathbf{B_r} = -\frac{r}{2} \frac{\partial \mathbf{B_z}}{\partial z}, \tag{1.4}$$

where r is the radial distance from the solenoid axis.

Further discussion and details of solenoids as focusing magnets in charged particle beams can be found in [9], [10].

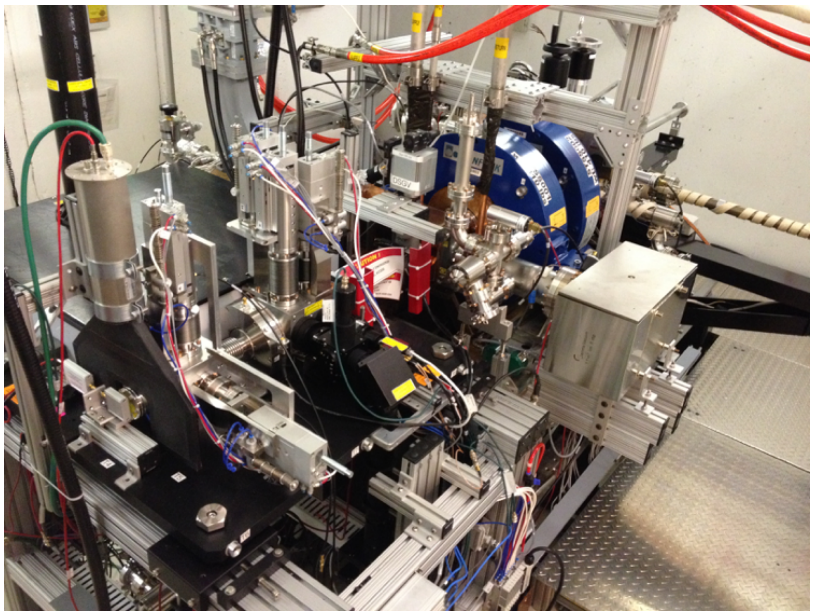

Figure 1.3: Bucking and main solenoid magnets (*in blue*) in the electron injector at FAST.

1.5.2 Quadrupole Magnets

As mentioned, quadrupole magnets (quad) are needed for quad-scans in order to focus or defocus a beam. Quadrupole magnets consist of four iron cores, wrapped in current-carrying wire, with a hyperbolic contour. This creates a magnet with alternating poles. At the center of the quad the Lorentz force is zero and the magnetic field lines become denser they approach the edges of the magnet. Thus, the Lorentz force is strongest near the pole tips. One can use the right-hand rule to determine the direction of the force on a charged particle passing through a quadrupole magnet. Assuming a configuration as shown in Fig. 1.4, a particle entering the quad in the plain of this paper would feel a force in the $+$ or $-$ x-direction (assuming the particle is travelling off-center along the $\pm$ x-direction, respectively). Conversely, a particle travelling off-center and into the plane of the paper would feel a force pushing the particle towards the center along the $\pm$ y-axis.

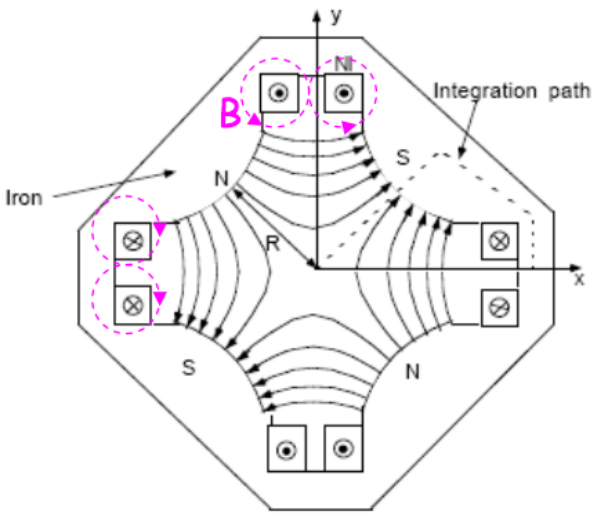

Figure 1.4: Drawing of the cross-section of a quadrupole magnet showing the magnetic field lines [11].

Quads can be thought of as analogous to optical lenses for focusing/defocusing a beam. In the example described above, the quad in 1.4 would focus an electron beam along the x-axis and defocus along the y-axis. If the quadrupole was arranged with opposite polarity, then the opposite would be true (focusing along the y-axis and defocusing along the x-axis). Since there exists this effect of always focusing in one plane and defocusing in the other, quads are typically arranged in pairs or triplets with alternating polarity (this is common in circular accelerators and has been coined F0D0 lattice meaning focusing, drift, defocusing, drift). Imagining a quad as an optical lens, it will impart a transverse momentum kick , that will increase linearly with the distance away from the center as seen in Fig. 1.5.

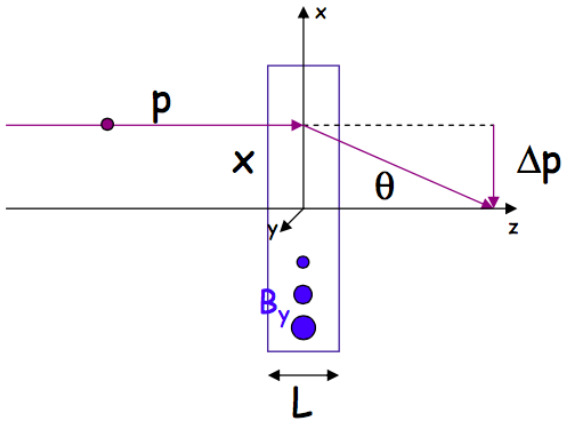

Figure 1.5: Side-view drawing of a quadrupole magnet. A particle with momentum p travels along the z-direction and feels a momentum kick (∇p) along the x-direction [11].

From Maxwell's equations for the magnetic field ($\nabla \cdot \mathbf{B} = 0$) and building to Laplace's equations for an electromagnetic (EM) potential ($\Delta V = 0$), it is possible to find solution's to Laplace's equation in $2D$ Cartesian coordinates to calculate the EM potential and, using a multipole expansion, calculate the magnetic field for a quadrupole magnet [11].

The solutions to Laplace's equation ($2D$ Cartesian) are:

$$\Delta V = 0 \Rightarrow \Delta V = \frac{d^2V}{dx^2} + \frac{d^2V}{dy^2} = 0 \tag{1.5}$$

Differentiating V will give the magnetic field:

$$B = -\nabla V_B(x, y) \tag{1.6}$$

Separating the solution in into the real (skew n-pole) and imaginary (normal n-pole) parts:

$$Re[V_n(x, y)] = -\frac{cp}{e}\sum_{m=0}^{n/2}(-1)^m(a_n + b_n)\frac{x^{n-2m}}{(n-2m)!}\frac{y^{2m}}{(2m)!} \tag{1.7}$$

$$Im[V_n(x, y)] = -\frac{cp}{e}\sum_{m=0}^{(n-1)/2}(-1)^m(a_n - b_n)\frac{x^{n-2m-1}}{(n-2m-1)!}\frac{y^{2m+1}}{(2m+1)!}, \tag{1.8}$$

where c is the speed of light, p is the momentum of the particles, and e is the electric charge of the particle.

In the case of the multipole expansion for quadrupoles, $n = 2$ and so the real and imaginary parts become:

$$Re(V) = (a_2 + b_2)\frac{x^2 - y^2}{2} \tag{1.9}$$

$$Im(V) = (a_2 - b_2)xy \tag{1.10}$$

The normal quadrupole potential is then:

$$V_2 = -\frac{cp}{e}(a_2 - b_2)xy \tag{1.11}$$

Differentiating gives the magnetic field in the transverse planes:

$$B_x = -\frac{dV_2}{dx} = \frac{cp}{e}(a_2 - b_2)y \tag{1.12}$$

$$B_y = -\frac{dV_2}{dy} = \frac{cp}{e}(a_2 - b_2)x \tag{1.13}$$

The quantity $(a_2 - b_2)$ is associated with the quadrupole field strength (k):

$$(a_2 - b_2) = \frac{cp}{e}\frac{dB_y}{dx} = k_x \tag{1.14}$$

$$(a_2 - b_2) = \frac{cp}{e}\frac{dB_x}{dy} = k_y \tag{1.15}$$

It is the quadrupole field strength k that is generally quoted in accelerator physics when discussing quad-scans. As mentioned previously, quads can be thought of as analogous to optical lenses and so k is thought of as a focusing strength. The focal length for a quadrupole magnet is [11]:

$$\frac{1}{f} = \frac{cp}{e}gL = \frac{gL}{B\rho}, \tag{1.16}$$

where (in one plane) g is the magnetic field gradient, L is the effective length of the quadrupole, and $B\rho$ is the magnetic rigidity [12]:

$$g_x = \frac{dB_y}{dx} \tag{1.17}$$

$$L_x = \frac{\int_{-\infty}^{\infty} \frac{dB_y}{dx} dz}{\frac{dB_y}{dx}} \tag{1.18}$$

$$B\rho = \frac{eB}{cp} \tag{1.19}$$

Finally, the quadrupole focusing strength may then be written as:

$$k\,(m^{-2}) = \frac{1}{fL} = \frac{eg}{pc} = 0.2998\frac{g\,(T/m)}{\beta E\,(GeV)}, \tag{1.20}$$

where $\beta = \frac{v}{c}$ (the Lorentz factor) and E is the beam energy.

At FAST, in the low energy beamline, there are twelve quads that are a part of the main beamline components (there are several others along the beamline including skew quadrupoles, chicane quadrupoles). A drawing of the section of the low-energy beamline, with locations of the quads (green arrows) TPMs (red arrows), is presented in 1.6. These quads, which can be seen in Fig. 1.7, are air-cooled and reach a maximum integrated field of 1.1 T when excited by a 9.0 A current and have a focusing strength of 6.6 for a 50 MeV beam [13].

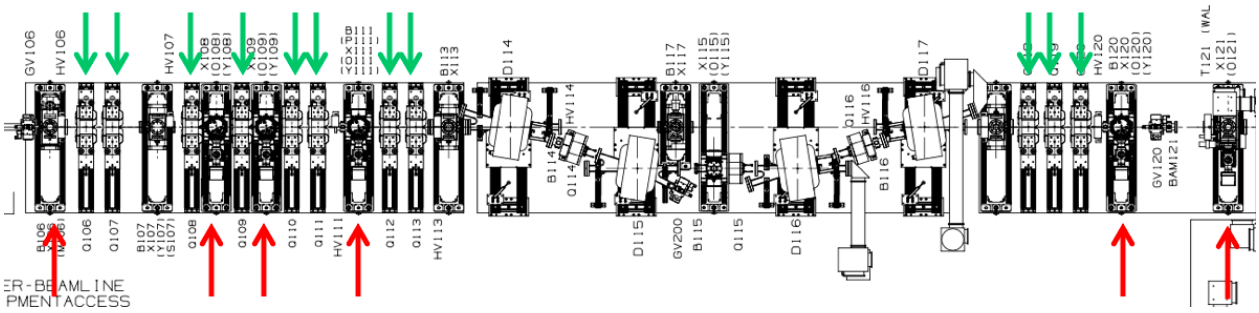

Figure 1.6: Drawing of the FAST low-energy beamline showing location of quads (green arrows) and TPMs (red arrows).

The ACNET control system, located at FAST, is used to operate the electron injector controls and measures the current admitted to the quads [13]. To calculate the magnetic field strength from the current, an equation derived from simulation and the construction of the linac is used:

$$k = \frac{10.135 \cdot 40 \cdot I}{1.8205 \cdot p}, \tag{1.21}$$

where I is the quad current (A) and p is the momentum (MeV/c).

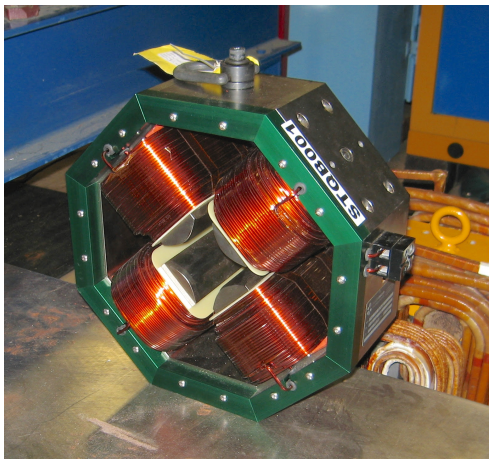

Figure 1.7: Image of a FAST low-energy beamline quadrupole magnet.

1.5.3 Transverse Profile Monitors

While scanning the quadrupole field strength, the beam must be imaged on a screen and the beam size recorded for each quadrupole field strength setting ($k - value$) in order to calculate the transverse beam emittance. Quad-scans have been implemented at FAST with the use of transverse profile monitors (TPM). TPMs measure the transverse beam intensity distributions within the 9 imaging stations with 6-port vacuum crosses along the beamline. These devices include internal vacuum hardware, optical transport, and pneumatic mechanical actuators [14].

The TPMs, which are actually two 2-position actuators that are piggy-backed, are able to insert or retract to four positions: cage (or the "out" position), scintillator screen, OTR screen, and target [14]. A closeup of the holder within the TPM assembly is shown in Fig. 1.8 with the four possible positions.

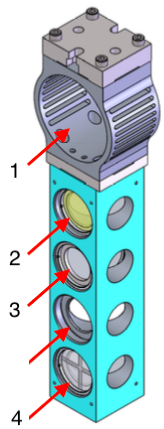

Figure 1.8: Closeup of a TPM holder and the four possible positions: (1) cage (or the "out" position), (2) scintillator screen, (3) OTR screen, and (4)target. The space between (3) and (4) is blank.

The red arrows specify the direction of propagation of the beam and the numbers correspond to the four positions:

1. Cage - this is the "out position". When the TPM's are not in use, this is the position. The opening is enclosed by an RF shield and the unperturbed beam passes through this opening.

2. Scintillator screen - there are one of two sources of scintillation light for viewing the beam size in each monitor:

   - A Ce-doped 250 μm thick crystalline yttrium aluminum garnet (YAG) screen.
   - A 100 μm thick crystalline lutetium-yttrium oxyorthosilicate (LYSO) screen.

3. A 25 μm thick Al screen for optical transition radiation (OTR) production.

4. A target screen for calibration of the 5-megapixel charged coupling device (CCD) cameras, which have a 1σ resolution of $\leq$ 20 μm.

There also exists an empty space between the OTR and target positions which allows either a right-handed or left-handed configuration. The configuration in Fig. 1.8 is for a right-handed TPM, where the optical light is transported perpendicular (and to the right) to the path of the beam. If a left-handed configuration is needed, then the holder is rotated 180° (vertically) and this allows for shifting the the screens into their proper places. In other words, the *same* holder can be used for a configuration in which the optical light from the screens is transported either to the right *or* the left of the beam path without needing two differently oriented holders.

Figure 1.9 shows the full TPM setup, with actuator, holder, and CCD camera, as well as a closeup on the region containing the holder from Fig. 1.8. Behind the YAG and OTR screens are Si:Al mirrors at 45° with respect to the beam path. The optical light is bent and send towards a second 45° mirror which then transports the light to the CCD camera for imaging of the beam. The beam size is measured in pixels and, with the use of the target screen, it is possible to calibrate the cameras for beam size measurement. At FAST, the calibration factor for measuring the beam size with the CCD is 9.3 μm per pixel.

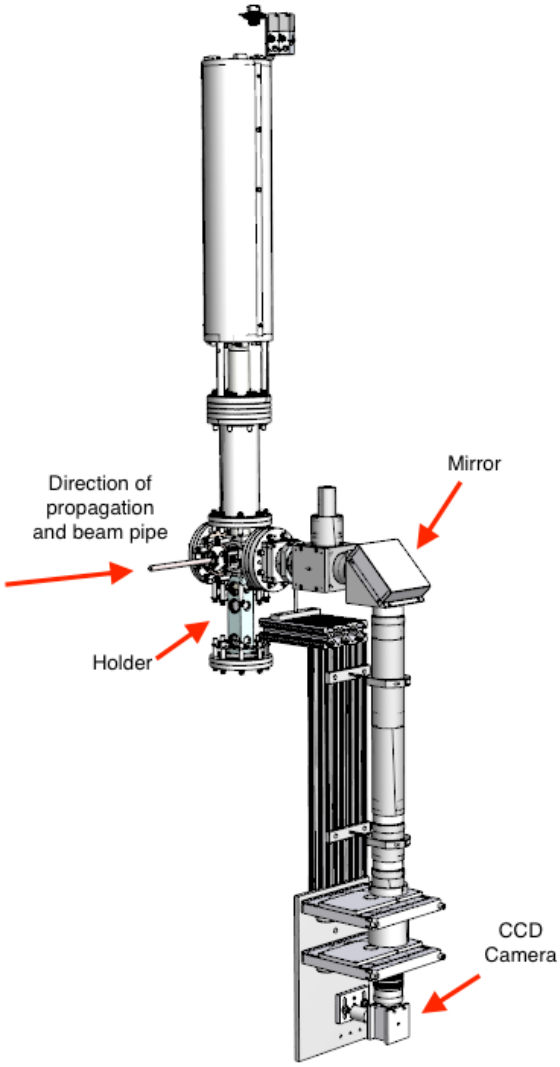

Figure 1.9: A full $3D$ drawing of the TPM station showing the direction of propagation of the beam, holder, second mirror, and CCD camera.

CHAPTER 2

TRANSVERSE BEAM EMITTANCE

2.1 Introduction

Beam emittance is a parameter describing the quality of a charged particle beam. In short, emittance can be thought of as the volume in phase space occupied by the beam. Of particular interest is the transverse emittance. The beam emittance provides information of the ability of a beam to be transported over long distances or to be focused into a tight space. In the following sections several beam parameters will be discussed beginning with phase space, the beam ellipse, and finally two descriptions of the transverse beam emittance.

2.2 Beam Dynamics in Phase Space

In a particle accelerator, electromagnetic fields are used to accelerate the charged particles. Electric fields are used to accelerate the particles and magnetic fields are using for bending and/or focusing or defocusing. The equations of motion in a particle accelerator can be described Hamiltonian's equations of motion:

$$\begin{cases} \dot{q}_i = \dfrac{\partial H}{\partial p_i} \\ \\ \dot{p}_i = -\dfrac{\partial H}{\partial q_i} \end{cases}, \tag{2.1}$$

where H is the Hamiltonian and a function of the position, conjugate momenta, and time $[H = H(\dot{q}, \dot{p}, t)]$ and $i = 1, \cdots, r$, with r representing the number of degrees of freedom. Using these conjugate coordinates, a canonical phase space may be described by the $2r$-dimensional space [15].

A single species beam is comprised of N particles and so the system contains $3N$ degrees of freedom. The motion of the particles in a beam can therefore be characterized by a six-dimensional canonical vector:

$$\mathbf{X} = (\mathbf{x}, \mathbf{p}), \tag{2.2}$$

which is described by the spatial coordinate $\mathbf{x}$ and $\mathbf{p}$:

$$\begin{cases} \mathbf{x} = (x, y, z) \\ \\ \mathbf{p} = (p_x, p_y, p_z) \end{cases}, \tag{2.3}$$

where x, y represent the displacement from the design orbit and z is the coordinate along the reference orbit [16]. To reiterate, the equations of motion in an accelerator are written "around" the trajectory of a reference "orbit" or particle.

In practice, the accelerator physics community use geometrical coordinates instead of the canonical phase space (sometimes called *tracespace*, though this paper will continue to use phase space). The coordinates describing particle motion are now:

$$\mathbf{X}(z) = (x, x', y, y', l, \delta), \tag{2.4}$$

which are defined in the following way [16]:

- x represents the horizontal displacement from the reference orbit.
- y represents the vertical displacement from the reference orbit.

- $x' = \frac{p_x}{p_z}$ represents the horizontal slopes with respect to the reference trajectory (also called the divergence).
- $y' = \frac{p_y}{p_z}$ represents the vertical slopes with respect to the reference trajectory (divergence).
- l is the longitudinal displacement from the reference particle.
- $\delta = \frac{\Delta p}{p}$ is the relative momentum deviation from the reference momentum.

A graphical example of the accelerator coordinate system, along with the reference particle and reference trajectory, is given in Fig. 2.1 [16].

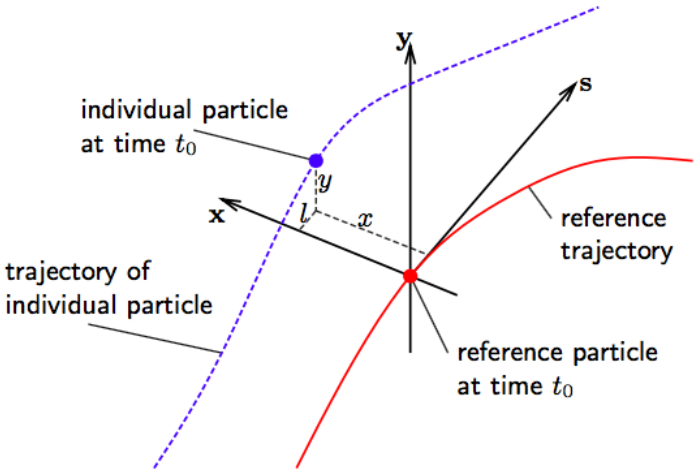

Figure 2.1: Coordinate system in an accelerator showing the reference particle and trajectory along with the properties and trajectory of an individual particle [16].

According to Liouvilles theorem, and with the use of the Hamiltonian equations for conservative systems, under the influence of conservative forces the phase space density of the particles remains invariant. There are many detailed discussions of Liouvilles theorem and for further reading in its application to particle accelerator physics and beam emittance please refer to [15], [16]. As a consequence of Liouvilles theorem, the motion of a beam, and in turn the motion of many particles in the phase space, may be tracked anywhere along the beam line with the use of a transfer matrix in the 6D phase space:

$$\mathbf{X}(z)_f = \mathbf{R} \cdot \mathbf{X}(z)_i, \tag{2.5}$$

where the subscripts i and f represent the initial and final positions with respect to the a reference trajectory. This equation can be expanded to full matrix form:

$$\begin{pmatrix} x_f \\ x'_f \\ y_f \\ y'_f \\ l_f \\ \delta_f \end{pmatrix} = \begin{pmatrix} R11 & R12 & R13 & R14 & R15 & R16 \\ R21 & R22 & R23 & R24 & R25 & R26 \\ R31 & R32 & R33 & R34 & R35 & R36 \\ R41 & R42 & R43 & R44 & R45 & R46 \\ R51 & R52 & R53 & R54 & R55 & R56 \\ R61 & R62 & R63 & R64 & R65 & R66 \end{pmatrix} = \begin{pmatrix} x_i \\ x'_i \\ y_i \\ y'_i \\ l_i \\ \delta_i \end{pmatrix} \tag{2.6}$$

Using the quad-scan technique only the transverse properties can be measured and calculated, reducing the phase space to a 4D system in which l and δ are excluded. In many cases it also assumed that no coupling exists in the transverse plane, such that $\mathbf{R}$ is a 2×2 block diagonal matrix and so the system is reduced again to two, 2D transverse planes: (x, x') and (y, y'):

$$\begin{cases} \begin{pmatrix} x_f \\ x'_f \end{pmatrix} = \begin{pmatrix} R11 & R12 \\ R21 & R22 \end{pmatrix} \begin{pmatrix} x_i \\ x'_i \end{pmatrix} \\ \begin{pmatrix} y_f \\ y'_f \end{pmatrix} = \begin{pmatrix} R33 & R34 \\ R43 & R44 \end{pmatrix} \begin{pmatrix} y_i \\ y'_i \end{pmatrix} \end{cases} \tag{2.7}$$

Beam emittance and the various parameters in terms of the horizontal and vertical planes will therefore assume no coupling for the time being. Analysis of the 4D phase space and the cross-plane coupling term is given in Chapter 5.

2.3 Beam Ellipse

As mentioned in the previous section, Liouvilles theorem states that the area in phase space comprised of charged particles will remain constant under the influence of conservative forces. Accelerator physicists tend to think of these particles as being enclosed by an ellipse and it is the area of the ellipse which is called the beam emittance, ϵ. While the focusing and defocusing elements along a beamline will distort the shape of this ellipse, the area will not change (thus satisfying Liouvilles theorem).

One analogy is to imagine a balloon as representing the beam. Quadrupoles focus or defocus a beam and when the beam is focused in one plane, it will defocus in the other (and vice versa). The analogy to the balloon is that if a balloon is squeezed at the waist horizontally (focus) it will stretch vertically (defocus) and vice versa.

For simplicity, the relevant equations throughout this chapter will analyze only the horizontal plane (x). For analysis of the vertical plane (y), simply substitute any x with y.

The beam ellipse is comprised of three independent parameters and one dependent parameter: α_x, β_x, and γ_x are the Courant-Snyder parameters (sometimes called Twiss parameters) and ϵ_{g_x} is the geometrical emittance. A drawing of the ellipse can be found in Fig. 2.2.

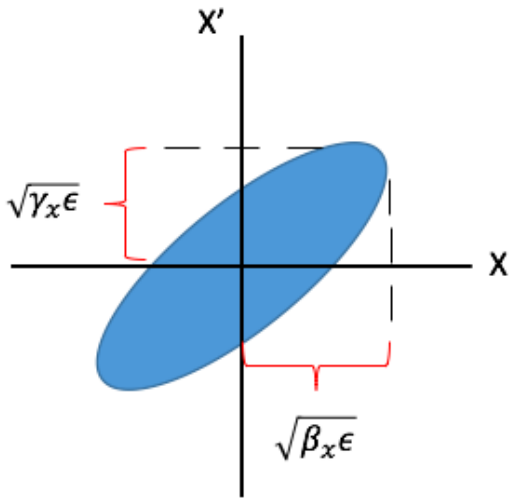

Figure 2.2: Drawing of the beam ellipse in horizontal phase space.

The equation of the beam ellipse is:

$$\epsilon_{g_x} = \gamma_x x^2 + 2\alpha_x x x' + \beta_x x'^2 \tag{2.8}$$

A derivation of the beam ellipse equation and its relationship to the Courant-Snyder parameters can be found in [16].

The mathematical definitions of the Courant-Snyder parameters are:

$$\alpha_x = -\frac{\langle x x' \rangle}{\epsilon_{g_x}} \tag{2.9}$$

$$\beta_x = \frac{\langle x^2 \rangle}{\epsilon_{g_x}} \tag{2.10}$$

$$\gamma_x = \frac{1+\alpha_x^2}{\beta_x} = \frac{\langle x'^2 \rangle}{\epsilon_{g_x}} \tag{2.11}$$

Comparing Eq.s (2.9)-(2.11) with Fig. 2.2 shows the relationship between the beam ellipse and the Courant-Snyder parameters: $\sqrt{\beta_x \epsilon_{g_x}}$ corresponds to the beam half-width, $\sqrt{\gamma_x \epsilon_{gx}}$ corresponds to the beam half-divergence, and α_x is the correlation term between x and x'. For $\alpha_x > 0$ the beam is converging, for $\alpha_x < 0$ the beam is diverging, and for $\alpha_x = 0$ the beam has a minimum or maximum [17].

The quantities $\langle x^2 \rangle$, $\langle x'^2 \rangle$, and $\langle x x' \rangle$ are the second-order moments of the beam distribution:

$$\langle x^2 \rangle = \frac{\int_0^\infty x^2 f(u) du}{\int_0^\infty f(u) du} \tag{2.12}$$

These second-order moments are the variances of the beam distribution in and . Taking the square root of these quantities yields the root mean square (RMS) beam size, divergence, and cross-correlational term in the transverse planes:

$$x_{rms} = \sqrt{\frac{1}{N} \sum_{i=1}^{N} x_i^2} \tag{2.13}$$

With this statistical description of the beam in hand, the 2×2 horizontal beam matrix, which is a sub-matrix of the full 4D transverse beam matrix, may be defined as:

$$\sigma_{\mathbf{xx}} = \begin{pmatrix} \sigma 11 & \sigma 12 \\ \sigma 21 & \sigma 22 \end{pmatrix} = \epsilon_{g_x} \begin{pmatrix} \beta_x & -\alpha_x \\ -\alpha_x & \gamma_x \end{pmatrix} = \begin{pmatrix} \langle x^2 \rangle & \langle x x' \rangle \\ \langle x x' \rangle & \langle x'^2 \rangle \end{pmatrix} \tag{2.14}$$

Again, simply replacing x with y gives the vertical beam matrix. The measurable quantity that an experimenter records is the beam size (σ_x), which has the following relationships:

$$\sigma_{11} = \sigma_x^2 = \langle x^2 \rangle = \beta_x \epsilon_{g_x}, \tag{2.15}$$

with the remaining elements of the beam matrix being:

$$\sigma_{12} = \sigma_{21} = \langle xx' \rangle = -\alpha_x \epsilon_{g_x}, \tag{2.16}$$

$$\sigma_{22} = \langle x'^2 \rangle = \gamma_x \epsilon_{g_x}, \tag{2.17}$$

2.3.1 Transformation of the Beam Ellipse in Phase Space

As discussed previously, in particle beam dynamics the motion of many particles in phase space follow Liouvilles theorem, which states that under the influence of conservative forces the particle density in phase space remains constant [18]. As a beam propagates along a beamline its shape and orientation will change, but the area will remain invariant [19]. An advantage of the application of this theorem to the idea of beam emittance is that knowledge of the area in phase space occupied by the particles at the beginning of the beamline allows for the determination of the location and distribution of the beam at any place along the beamline without having to calculate the trajectory of each individual particle [18].

Figure 2.3 shows the evolution of the spot size and the transformation of the phase space ellipse of a diverging beam after passing through a focusing quad and then continuing along the z-direction in a drift space. The force of the kick from a quadrupole is opposite to the sign of the particle's position and proportional to the distance from the axis [19]. The slope of the trajectories of the particles within the beam ellipse reverse sign, leading to a converging beam. Without focusing elements, however, the beam continues to rotate through the beam waist and eventually diverges. As discussed in Chapter 1, a quadrupole magnet focuses in one plane, while it defocuses in the other. For this reason, a defocusing quad would follow shortly after a focusing quad and vice-versa (usually arranged in pairs or triplets).

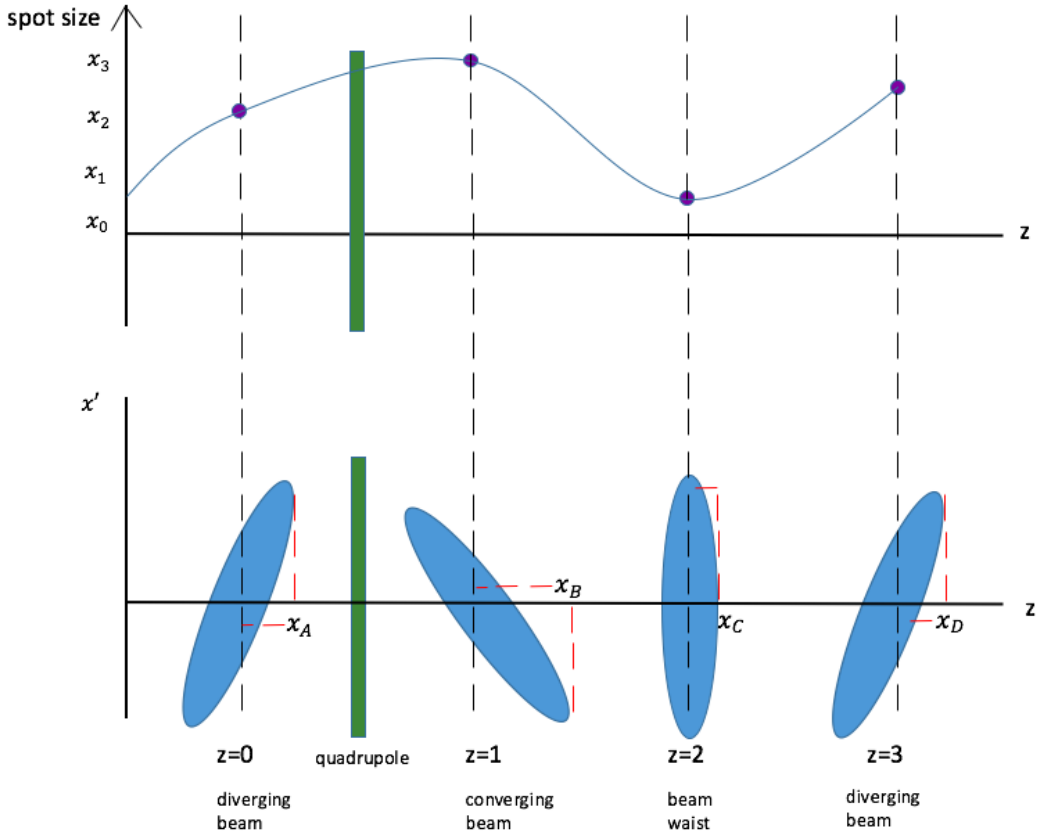

Figure 2.3: Drawing of the evolution of a divergent beam passing through a focusing quadrupole. Shown here is both the evolution of the beam spot size as well as the beam ellipse as it rotates through phase space.

2.4 Transverse Beam Emittance

Transverse beam emittance can be written in two ways, the RMS geometrical emittance (ϵ_{g_x}) and the normalized emittance (ϵ_{nx}), and it will be defined as the area of a distribution of particles that are bound by an ellipse in phase space. Once the components of the beam matrix are known, the geometrical emittance can be calculated:

$$\epsilon_{g_x} = \sqrt{det(\sigma_{\mathbf{xx}})} = \sqrt{\sigma_{11}\sigma_{22} - \sigma_{21}^2} \tag{2.18}$$

In practice, the quoted emittance is typically normalized with the beam energy. This allows for the comparison of a beams quality independent of the effects of acceleration [19]:

$$\epsilon_{nx} = \beta\gamma\epsilon_{gx}, \tag{2.19}$$

where β and γ are the relativistic velocity and Lorentz factor:

$$\beta = \frac{v}{c} \tag{2.20}$$

$$\gamma = \frac{1}{\sqrt{1-\beta^2}} \tag{2.21}$$

CHAPTER 3
BEAM PARAMETER MEASUREMENT BASED ON THE QUADRUPOLE SCAN TECHNIQUE

3.1 Introduction

The quadrupole scan (quad-scan) technique is a simple, effective, and well established method of estimating the transverse beam emittance and Courant-Snyder parameters of a charged particle beam. This chapter will discuss the theory and mathematics of quad-scans and, in particular, the two methods in which this technique is used: the Thin Lens approximation and thick lens model. The thin tens model is an approximation in which the quadrupole is treated as a thin lens, analogous to an optical thin lens. In the thick lens model, the geometrical thickness of the quadrupole, and therefore the effect of the magnetic field strength on the beam over the course of the effective length of the quad, are taken into account. General procedures for quad-scans will be discussed here and in Chapter 6 the specific methods and analytical tools used at FAST will be detailed.

The quad-scan technique is an indirect method for measuring transverse beam emittance with a minimum perturbation on the beam ellipse in the phase space. There are only two main components required for a quadrupole scan: a quadrupole magnet and a transverse profile monitor (TPM). As with all linac, there are multiple quads and TPMs to choose from. The general procedure of quad-scan is as follows: one chooses a single quadrupole and TPM to operate. The quadrupole magnet current is then scanned over a desired range and the beam size is recorded on the downstream imaging screen.

It is generally best to find the minimum beam size, or the beam waist (where the cross-correlation term $xx' = 0$), by scanning the quadruple. This is done by increasing or decreasing the quad current (i.e. scanning the quad current), which in turn scans the magnetic field. This is particularly important when analyzing the data with the thin lens approximation, since the beam size (squared) must be plotted as a function of the magnetic field strength, which generates a parabola. A 2nd order polynomial function is the fit to the data. For a good fit, with a roughly symmetric parabola, it is necessary to pass through the minimum beam size. Figure 3.1 is a flow chart showing the three *general steps* to follow when preforming a quad-scan. Details into the two methods of emittance calculation with the quad-scan technique will be given in the following chapters.

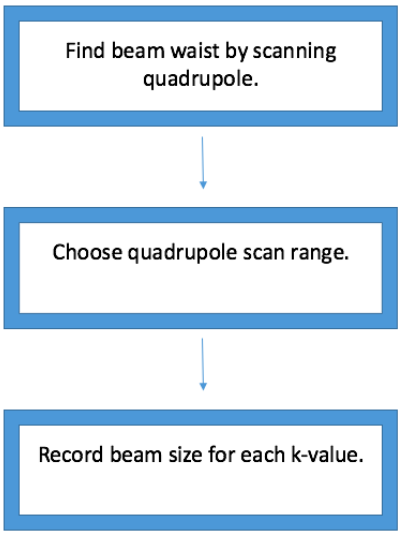

Figure 3.1: Basic flow chart showing the general quad-scan procedure.

3.2 Methods for Estimating Beam Emittance

Using the quad-scan technique, there are two methods for estimating the transverse beam emittance: the "thick lens" model and the "thin lens" approximation. The next three subsections will details the mathematical treatment of these methods.

3.2.1 Drift Space Transformation

In linear beam dynamics, the equations of motion of particle trajectories through a beam transport line can be reduced to that of a harmonic oscillator (where the bending radius of the reference trajectory is zero and no dispersion is created in the drift space). If the trajectory of a particle along a drift is in the z-direction, then the solutions to the equations of motion can be expressed in matrix form as [18]:

$$\begin{pmatrix} x(z) \\ x'(z) \end{pmatrix} = \begin{pmatrix} 1 & L \\ 0 & 1 \end{pmatrix} \begin{pmatrix} x(z_0) \\ x'(z_0) \end{pmatrix}, \tag{3.1}$$

where L is the drift length ($L = z - z_0$), z represents the position of the TPM along the beamline, and z_0 represents the end edge of the quadrupole magnet. The drift space may then be written in a matrix form representing the drift space transfer matrix:

$$\mathbf{S} = \begin{pmatrix} 1 & L \\ 0 & 1 \end{pmatrix} = \begin{pmatrix} S_{11} & S_{12} \\ S_{21} & S_{22} \end{pmatrix} \tag{3.2}$$

Figure 3.2 shows a graphical example of the drift length and its relationship to the quad and TPM. At this point, one must choose whether to progress to the thin lens approximation or the thick lens model, since their transfer matrices and the method of calculating emittance difference from this point on.

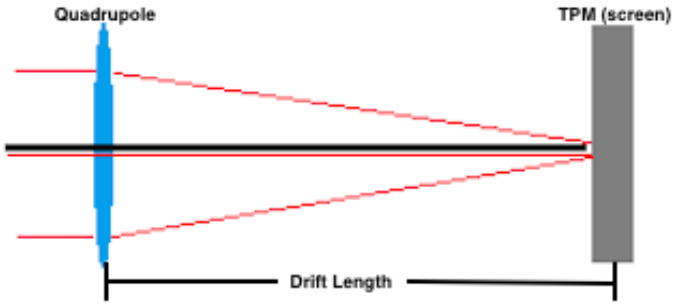

Figure 3.2: Graphical example of the drift length (L) between a quadrupole magnet and TPM.

3.2.2 "Thin Lens" Approximation

The mathematics that comprise emittance calculations using the quad-scan technique revolve around transfer matrices. Repeated multiplication and manipulation of matrices can be very tedious and it is no different when performing emittance calculations. For this reason, many physicists use computers to calculate the properties of beam dynamics. In some cases, it may be desirable to calculate a small set of properties or beam elements analytically using approximations. If this is the case when it comes to calculating transverse emittance, then the Thin Lens approximation is generally used [18]. More importantly, the "thin lens" approximatino is valid only when the length of the quadrupole magnet is small compared to its focal length. This is analogous to an optical thin lens, as shown in Fig. 3.3.

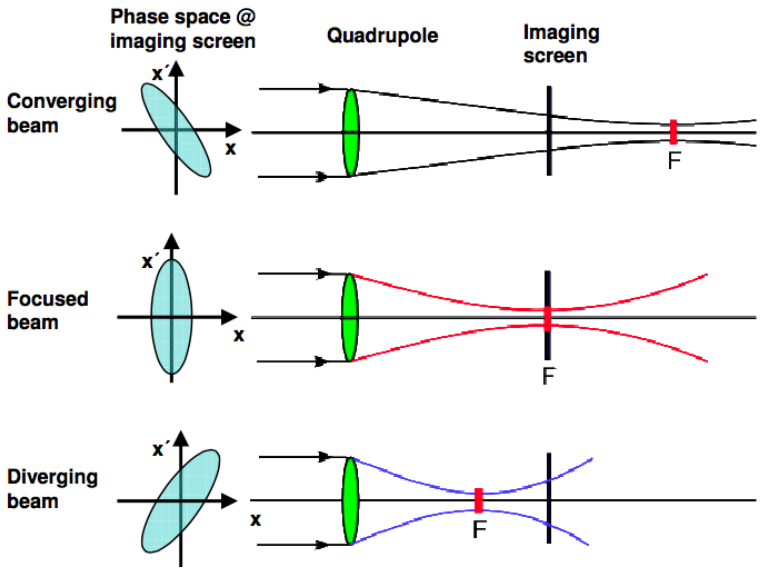

Figure 3.3: Depiction of a converging, focused, and diverging beam and the focal points as they pass through a quadrupole magnet. In the "thin lens" approximation, the quad acts as a thin lens - analogous to a thin lens in optics [20].

The length of the quad then goes to zero (hence the "thin lens" nomenclature) and the focal length is constant [18]:

$$l \ll f,\ l \to 0,\ \frac{1}{f} = kl = constant, \tag{3.3}$$

where k is the magnetic field strength of the quadrupole and l is the effective length of the quadrupole. The transfer matrix of the quadrupole can then be written as:

$$\mathbf{Q} = \begin{pmatrix} Q_{11} & Q_{12} \\ Q_{21} & Q_{22} \end{pmatrix} = \begin{pmatrix} 1 & 0 \\ kl & 1 \end{pmatrix} \tag{3.4}$$

The quadrupole transfer matrices are identical other than the sign of the of the focal length:

$$\frac{1}{f} = \begin{cases} kl > 0 \rightarrow focusing \\ \\ kl < 0 \rightarrow defocusing \end{cases}$$

It is now possible to write the total transfer matrix ($R = SQ$) between the quad and the TPM:

$$\begin{pmatrix} x(z) \\ x'(z) \end{pmatrix} = \begin{pmatrix} S_{11} + kl \cdot S_{12} & S_{12} \\ S_{21} + kl \cdot S_{12} & S_{22} \end{pmatrix} \begin{pmatrix} x(z_0) \\ x'(z_0) \end{pmatrix} \tag{3.5}$$

Using the beam matrix of Chapter 2.2 and combining this with the total transfer matrix R, the beam matrix anywhere along the beamline is given by:

$$\sigma(z) = \mathbf{R}(z)\sigma(z_0)\mathbf{R^T}(z), \tag{3.6}$$

where T is the transpose operator.

Again, in terms of a quad-scan, $\sigma(z)$ represents the beam matrix at the TPM and $\sigma(z_0)$ represents the beam matrix at the entrance of the quad. As another reminder, for simplicity focus has been shifted to only the horizontal (x) components of the 2×2 beam matrix.

The first term in the resulting matrix from Eq. (3.5), which is the measurable quantity in a quad-scan (the beam size), is:

$$x = (S_{11} + kl \cdot S_{12})x_0 + S_{12}x'_0 \tag{3.7}$$

Squaring and averaging this term gives the first element of the beam matrix:

$$\sigma_{11} = \langle x^2 \rangle = (S_{11} + kl \cdot S_{12})^2 \langle x_0^2 \rangle + S_{12}^2 \langle x_0'^2 \rangle + 2S_{12}(S_{11} + kl \cdot S_{12}) \langle xx' \rangle \tag{3.8}$$

As a reminder, and so that it is easier to make the connection here, the beam matrix is related to the beam size, divergence, and cross-correlation terms by:

$$\sigma_{11} = \langle x^2 \rangle \tag{3.9}$$

$$\sigma_{12} = \sigma_{21} = \langle x'^2 \rangle \tag{3.10}$$

$$\sigma_{22} = \langle x'^2 \rangle \tag{3.11}$$

As discussed in Chapter 3.2, the procedure for quad-scans is to select a quadrupole magnet, scan the magnetic field strength, and measure the beam size on the TPM as it changes. So, for every k_i there exists a σ_{11i}. If an experimenter finds a beam waist and then scans an equal amount of data points on either side of the waste and then plots σ_{11} data as as a function of k, then it will be found that by applying a fitting function, such as a 2nd order polynomial fit, the data will follow a parabolic shape as shown in Fig. 3.4.

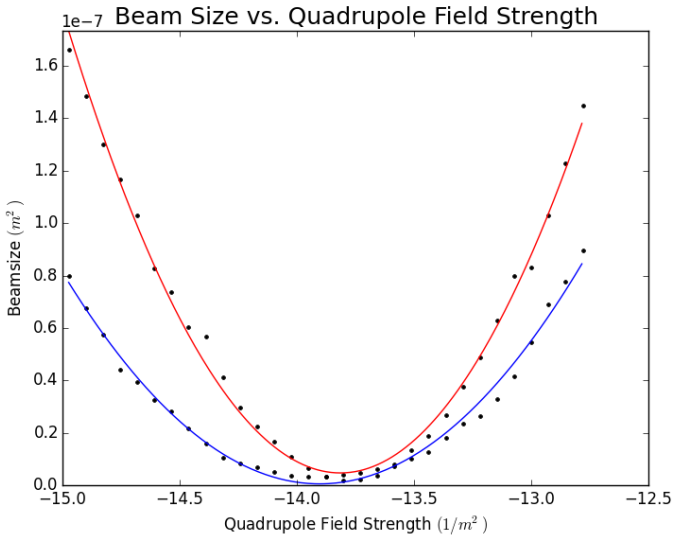

Figure 3.4: A plot of the beam size (squared) as a function of quadrupole field strength. The blue fit represents the horizontal plane and the red fit represents the vertical plane.

The standard form for the equation of a parabola is as follows:

$$y = ax^2 + bx + c \tag{3.12}$$

Expanding Eq. (3.8), collecting terms, and setting it equal to Eq. (3.12) while using the three coefficients from the polynomial fit, it is possible to solve for the beam matrix elements:

$$Ak^2 = \sigma_{11}k^2l^2S_{12}^2 \Rightarrow \sigma_{11} = \frac{A}{l^2S_{12}^2} \tag{3.13}$$

$$Bk = 2\sigma_{11}klS_{11}S_{12} + 2\sigma_{12}klS_{12}^2 \Rightarrow \sigma_{12} = \frac{B - 2\sigma_{11}lS_{11}S_{12}}{2lS_{12}^2} \tag{3.14}$$

$$C = \sigma_{11}S_{11}^2 + \sigma_{22}S_{12}^2 + 2\sigma_{11}S_{11}S_{12} \Rightarrow \sigma_{22} = \frac{C - \sigma_{11}S_{11}^2 - 2\sigma_{12}S_{11}S_{12}}{S_{12}^2}, \tag{3.15}$$

where the subscripts 0 have been dropped, though these beam matrix elements are still those at the entrance of the quadrupole.

The coefficients A, B, and C that are retrieved from the fit are then used to solve for the beam matrix elements. From here it is straightforward to calculate the geometrical and normalized emittances and Courant-Snyder parameters as discussed in Chapters 2.3 and 2.5.

3.2.3 "Thick Lens" Model

As the name suggests, this model treats the quadrupole magnet as a thick lens. There are several factors that differentiate the thick lens vs. thin lens, with two of the most notable being:

1. The dimensions of the quadrupole magnet are no longer ignored. If the effective length of the magnet is not negligible when compared to the focal length, then the thin lens approximation cannot be used.

2. The "thick lens" model is an exact linear model for the quadrupole matrix.

In addition to the two differences mentioned above, the quadrupole transfer matrix components are also described in another way. The focusing and defocusing quadrupole matrices for the thick lens model are (again, ignoring any coupling for simplicity and approaching the horizontal and vertical planes as 2×2 matrices):

$$\mathbf{Q}_f = \begin{pmatrix} \cos\phi & \frac{1}{\sqrt{|k|}}\sin\phi \\ -\sqrt{|k|}\sin\phi & \cos\phi \end{pmatrix} \tag{3.16}$$

$$\mathbf{Q}_d = \begin{pmatrix} \cosh\phi & \frac{1}{\sqrt{|k|}}\sinh\phi \\ \sqrt{|k|}\sinh\phi & \cosh\phi \end{pmatrix}, \tag{3.17}$$

where $\mathbf{Q}_f$ describes a focusing quadrupole ($k > 0$), $\mathbf{Q}_d$ describes a defocusing quadrupole ($k < 0$), and $\phi = \sqrt{|k|} \cdot l$. By convention, at FAST a positive quadrupole current corresponds to a positive k-value and a horizontally focusing quad.

The drift matrix elements remain the same and the total transfer matrix is now defined as:

$$\mathbf{R} = \mathbf{SQ} = \begin{pmatrix} S_{11}\cos\phi - S_{12}\sqrt{|k|}\sin\phi & \frac{S_{11}}{\sqrt{|k|}}\sin\phi + S_{12}\cos\phi \\ S_{12}\cos\phi - S_{22}\sqrt{|k|}\sin\phi & \frac{S_{21}}{\sqrt{|k|}}\sin\phi + S_{22}\cos\phi \end{pmatrix} \tag{3.18}$$

This is the transfer matrix for a focusing quadrupole. The transfer matrix for a defocusing quadrupole is the same, with the exception of replacing sine function and cosine function with their hyperbolic counterparts and replacing the subtraction of elements R_{11} and R_{12} with an addition. The transformation of the beam matrix through the beamline is the same

as Eq. (3.6). Also, as with the thin lens approximation, the reduced equation for the first element of the beam matrix is:

$$\sigma_{11} = \langle x^2 \rangle = R_{11}^2 \sigma_{11}^{(0)} + 2R_{11}R_{12}\sigma_{12}^{(0)} + R_{12}^2 \sigma_{22}^{(0)} \tag{3.19}$$

For many measurements of the σ_{11} for different quadrupole settings, the full transfer matrix is:

$$\begin{pmatrix} {\sigma_{11}}_s^{(a)} \\ {\sigma_{11}}_s^{(b)} \\ \vdots \\ {\sigma_{11}}_s^{(n)} \end{pmatrix} = \begin{pmatrix} R_{11}^{2(a)} & 2R_{11}^{(a)}R_{12}^{(a)} & R_{12}^{2(a)} \\ R_{11}^{2(b)} & 2R_{11}^{(b)}R_{12}^{(b)} & R_{12}^{2(b)} \\ \vdots & \vdots & \vdots \\ R_{11}^{2(n)} & 2R_{11}^{(n)}R_{12}^{(n)} & R_{12}^{2(n)} \end{pmatrix} \begin{pmatrix} {\sigma_{11}}_q \\ {\sigma_{12}}_q \\ {\sigma_{22}}_q \end{pmatrix} = \mathbf{A} \begin{pmatrix} {\sigma_{11}}_q \\ {\sigma_{12}}_q \\ {\sigma_{22}}_q \end{pmatrix}, \tag{3.20}$$

where the subscripts s and q represent the screen (TPM) and quad, respectively.

Eq. (3.20) is of the form $\mathbf{Ax} = \mathbf{b}$. There are more equations than unknowns (the matrix has more rows than columns) and so an exact solution cannot be found [21]. The goal is then to minimize the error by employing a least-squares fit, which is performed by inverting the curvature matrix $\mathbf{A}$:

$$\mathbf{x} = A^{-1}b \tag{3.21}$$

One benefit of using PYTHON for these calculations is that the polynomial fitting function from the NumPy scientific computing package is actually a least square fit and it returns a vector of coefficients that minimizes the squared error (PYTHON will be further explored in Chapter 6 [22]. The calculated elements of this vector are the three coefficients given in Eq's (3.9) - (3.11).

It is also possible to apply a least-squares fit for the thick lens model in PYTHON using the *numpy.linalg.lstsq* command, which returns the least-squares solution to a linear matrix equation [22]. The vector that is returned are simply the beam matrix elements at the quadrupole, from which the emittance can be solved for in the usual way using Eq. (2.18). This method of using a least-squares fit for determining the emittance gives a consistent and direct comparison of the "thin lens" vs. "thick lens" models.

CHAPTER 4

χ^2 DISTRIBUTION AND ERROR ANALYSIS

4.1 Introduction

Building upon the matrices and equations used to determine the transverse emittance from the thick lens model as described in Chapter 3, this chapter will give further details on the thick lens model and will now give consideration to error via the χ^2 distribution and least-squares fitting.

4.2 χ^2 Distribution

The χ^2 test gives some insight into the agreement between an observed distribution of measurements and an expected distribution (such as a Gaussian distribution of measurements) by a sum of squares with the general form [23]:

$$\chi^2 = \sum_{i=1}^{n} \left(\frac{observed\,value\ -\ expected\,value}{standard\,deviation} \right)^2 \tag{4.1}$$

This equation can be applied to various situations, including functions (such as the quadratic polynomial function which has been discussed):

$$\chi^2 = \sum_{i=1}^{n} \left(\frac{y_i - f(k, A, B, C)}{\delta_i} \right)^2, \tag{4.2}$$

where $f(k, A, B, C) = Ak^2 + Bk + C$.

As shown in Eq. (3.20), the equation is written as $\mathbf{Ax} = \mathbf{b}$, where to solve for the beam matrix elements $\vec{b}$, the matrix A must be inverted. Since there are i measurements of the beam size taken in a quad-scan and three elements in the transfer matrix per beam size, a $m \times n$ matrix remains. Since a $m \times n$ matrix is not square, it is not invertible and since inversion is required to solve for the beam matrix elements it is therefore required that the least-squares method is invoked. This gives a vector of estimated coefficients (namely, the beam matrix elements):

$$\mathbf{Ax} = \mathbf{b} \Rightarrow \mathbf{x} = \left(\mathbf{A^T A}\right)^{-1} \mathbf{A^T b} \tag{4.3}$$

4.3 Error Analysis

With some basic χ^2/least-squares formalism in hand, it is now possible to directly apply this technique to the thick lens model using the methods described in [24]. This technique allows for the calculation of the horizontal and vertical transverse beam emittance, Courant-Snyder parameters, the errors on these quantities, and the covariance terms at a specific quadrupole magnet. In the quad-scan method that has been employed at FAST a single quadrupole magnet and TPM are selected, separated by a drift, and the magnetic field strength k is scanned over a specified range while the transverse beam size (in the x and y planes) is measured on the TPM for each k-value. For each $i'th$ measurement there is an equivalent transfer matrix $\mathbf{R}(i)$, RMS beam size $\sigma_x(i)$, and estimated error on the beam size $\delta_x(i)$.

The first element of the beam matrix, namely the square of the RMS beam size, and the measurement error for a given measurement are given by:

$$\sigma_{11}(i) = \sigma_x^2(i) = \langle x^2 \rangle \tag{4.4}$$

$$\delta(i) = 2\sigma_x(i)\delta_x(i), \tag{4.5}$$

where σ_{11} is the first element of the beam matrix, or the squared RMS beam size and the δ is the measurement error on this term:

$$\delta(i) = d\sigma_{11}(i) = 2\sigma_x d\sigma_x \;\rightarrow\; d\sigma_x \equiv \delta_x(i) \tag{4.6}$$

As mentioned, the goal is to calculate the specified beam matrix parameters by predicting the beam matrix elements $\left(\sigma_{nm}^{(0)}\right)$ at the quadrupole. It is then possible to construct a χ^2 distribution for a set of n measurements:

$$\chi^2 = \sum_{i=1}^{n} \left(\frac{\sigma_x(i) - \left(R_{11}^2(i)\sigma_{11}^{(0)} + 2R_{11}(i)R_{12}(i)\sigma_{12}^{(0)} + R_{12}^2(i)\sigma_{22}^{(0)} \right)}{\delta(i)} \right)^2 \tag{4.7}$$

It is now possible to write this equation in matrix form for the value of $\sigma^{(0)}$ in which χ^2 is minimized:

$$\begin{pmatrix} \sum \frac{R_{11}^2(i)\sigma(i)}{\delta^2(i)} \\ \sum \frac{2R_{11}(i)R_{12}(i)\sigma(i)}{\delta^2(i)} \\ \sum \frac{R_{12}^2(i)\sigma(i)}{\delta^2(i)} \end{pmatrix} = \begin{pmatrix} \sum \frac{R_{11}^4(i)}{\delta^2(i)} & \sum \frac{2R_{11}^3R_{12}(i)}{\delta^2(i)} & \sum \frac{R_{11}^2(i)R_{12}^2(i)}{\delta^2(i)} \\ \sum \frac{2R_{11}^3R_{12}(i)}{\delta^2(i)} & \sum \frac{4R_{11}^2R_{12}^2(i)}{\delta^2(i)} & \sum \frac{2R_{11}R_{12}^3(i)}{\delta^2(i)} \\ \sum \frac{R_{11}^2(i)R_{12}^2(i)}{\delta^2(i)} & \sum \frac{2R_{11}R_{12}^3(i)}{\delta^2(i)} & \sum \frac{R_{12}^4(i)}{\delta^2(i)} \end{pmatrix} = \begin{pmatrix} \sigma_{11}^{(0)} \\ \sigma_{12}^{(0)} \\ \sigma_{22}^{(0)} \end{pmatrix} \tag{4.8}$$

This equation is the now familiar $\mathbf{Ax} = \mathbf{b}$, where $\mathbf{A}$ is the *curvature matrix*, $\mathbf{x}$ is the *coefficient matrix* (the vector containing the beam matrix elements at the quadrupole), and

b is the matrix containing the sum of the product of the measured beam sizes and the transfer matrix elements. In order to find a solution for **x**, the inverse of A is taken (called the *error matrix*) and is then multiplied by **b**:

$$\mathbf{x} = A^{-1}b \tag{4.9}$$

To show this explicitly, the curvature matrix may be written as:

$$\mathbf{A} = \begin{pmatrix} a & 2b & c \\ 2b & 4c & 2d \\ c & 2d & e \end{pmatrix} \tag{4.10}$$

The error matrix now has the solution:

$$\mathbf{A^{-1}} = \frac{1}{det(\mathbf{A})} \begin{pmatrix} 4(ce-d^2) & -2(be-cd) & 4(bd-c^2) \\ -2(be-cd) & (ae-c^2) & -2(ad-bc) \\ 4(bd-c^2) & -2(ad-bc) & 4(ac-b^2) \end{pmatrix} \tag{4.11}$$

Again, by taking the product of $(\mathbf{A^{-1}b})$, the beam matrix elements of the coefficient matrix $\vec{x}$ are revealed and the transverse horizontal and vertical emittances and Courant-Snyder parameters can then be calculated in the usual way.

Additionally, the matrix elements of the error matrix give the error-estimates for the experimental uncertainties on the beam matrix elements. The diagonal elements are the squares of the errors and the off-diagonal elements are the covariance terms [24]:

$$A^{-1}_{11} = \delta^2_{11} \tag{4.12}$$

$$A_{22}^{-1} = \delta_{12}^2 \tag{4.13}$$

$$A_{33}^{-1} = \delta_{22}^2 \tag{4.14}$$

$$A_{12}^{-1} = \delta_{11,12} \tag{4.15}$$

$$A_{13}^{-1} = \delta_{11,22} \tag{4.16}$$

$$A_{23}^{-1} = \delta_{12,22} \tag{4.17}$$

Using computer codes, errors of the emittance and Courant-Snyder parameters are directly estimated from Eqs. (4.12) (4.17) [16]. A function f can then be defined as:

$$f = \begin{pmatrix} \beta_x \\ \alpha_x \\ \epsilon_{g_x} \end{pmatrix} = \begin{pmatrix} \frac{a_1}{\sqrt{a_1 a_3 - a_2^2}} \\ -a_2\sqrt{a_1 a_3 - a_2^2} \\ \sqrt{a_1 a_3 - a_2^2} \end{pmatrix}, \tag{4.18}$$

where a_i are the elements of the vector $\vec{x}$ in Eq. (4.8):

$$a_1 = \sigma_{11} \tag{4.19}$$

$$a_2 = \sigma_{12} \tag{4.20}$$

$$a_3 = \sigma_{22} \tag{4.21}$$

Next, the matrix C may be defined as the inverse of the product of the curvature matrix:

$$\mathbf{C} = \left(\mathbf{A^T A}\right)^{-1} \tag{4.22}$$

The diagonal elements of the $\mathbf{C}$ matrix are the variances of a_i and the off-diagonal elements are the covariance terms [16]. Using Eq. (4.18) and (4.22), it is possible to calculate the errors on the emittance and Courant-Snyder parameters. The diagonal elements of the error matrix $\sigma^2(f)$ in Eq. (4.23) contain the squared errors of the emittance and Courant-Snyder parameters:

$$\sigma(\mathbf{f})^{\mathbf{2}} = \left(\nabla_{\mathbf{a}}\mathbf{f}\right)^{\mathbf{T}} \mathbf{C} \left(\nabla_{\mathbf{a}}\mathbf{f}\right) = \begin{pmatrix} \sigma^2_{\beta_x} & \dots & \dots \\ \dots & \sigma^2_{\alpha_x} & \dots \\ \dots & \dots & \sigma^2_{\epsilon_{x\,g}} \end{pmatrix} \tag{4.23}$$

Explicitly, the gradient of the scalar function f is give as:

$$\nabla_{\mathbf{a}}\mathbf{f} = \begin{pmatrix} \frac{\partial \beta_x}{\partial a_1} & \frac{\partial \alpha_x}{\partial a_1} & \frac{\partial \epsilon_{x\,g}}{\partial a_1} \\ \frac{\partial \beta_x}{\partial a_2} & \frac{\partial \alpha_x}{\partial a_2} & \frac{\partial \epsilon_{x\,g}}{\partial a_2} \\ \frac{\partial \beta_x}{\partial a_3} & \frac{\partial \alpha_x}{\partial a_3} & \frac{\partial \epsilon_{x\,g}}{\partial a_3} \end{pmatrix}, \tag{4.24}$$

where the a_i terms are given in Eq. (4.19) Eq. (4.21). This equation is readily solved via computer codes and is the equivalent to the general equation for determining the squared error of a function $g(x_1, x_2, \dots, x_n)$ via error propagation [16]:

$$\sigma^2(g) = \sum_{i=1}^{n} \left(\frac{\partial g}{\partial x_i}\right)^2 \sigma^2_{x_i} + \sum_{i=1}^{n} \sum_{j=1,\, j\neq i}^{n} \frac{\partial g}{\partial x_i} \frac{\partial g}{\partial x_j} cov(i,j) \tag{4.25}$$

CHAPTER 5

ANALYSIS ON CROSS-PLANE COUPLING

5.1 Introduction

In the previous chapters, the beam emittance analysis assumed no cross-coupling between the horizontal and vertical planes for the sake of simplicity. If Gaussian fits are used to measure the beam size in the transverse plane, then the fits are applied to 2D projections of a 3D object and the cross-plane coupling term $\langle xy \rangle$ cannot be properly measured. Coupling between the transverse planes will tilt the image of the beam on the screen and the calculated emittance will be larger than it actually is (again, due to the beam size measurement from the projections in 2D). To measure the coupling term and apply analysis of the four dimensional phase space, a statistical approach (RMS) must be used, which will be discussed extensively in this chapter.

5.2 4D Beam Parameters

Expanding the 2D analysis of the transverse planes to the 4D phase space, the 4D beam matrix may now be written in terms of the second-moments as [25], [16]:

$$\sigma^{\mathbf{4D}} = \begin{pmatrix} \langle x^2 \rangle & \langle xx' \rangle & \langle xy \rangle & \langle xy' \rangle \\ \langle xx' \rangle & \langle x'^2 \rangle & \langle x'y \rangle & \langle x'y' \rangle \\ \langle xy \rangle & \langle x'y \rangle & \langle y^2 \rangle & \langle yy' \rangle \\ \langle xy' \rangle & \langle x'y' \rangle & \langle yy' \rangle & \langle y'^2 \rangle \end{pmatrix} = \begin{pmatrix} \sigma_{11} & \sigma_{12} & \sigma_{13} & \sigma_{14} \\ \sigma_{21} & \sigma_{22} & \sigma_{23} & \sigma_{24} \\ \sigma_{31} & \sigma_{32} & \sigma_{33} & \sigma_{34} \\ \sigma_{41} & \sigma_{42} & \sigma_{43} & \sigma_{44} \end{pmatrix}, \tag{5.1}$$

combining the six independent beam matrix elements from the transverse planes with the four independent cross-plane coupling beam matrix elements.

It is convenient to write this 4×4 matrix as a 2×2 matrix, with each element of the matrix being itself a 2×2 sub-matrix as shown on the right-hand side of the Eq. (5.2):

$$\sigma^{\mathbf{4D}} = \begin{pmatrix} \sigma_{xx} & \sigma_{xy} \\ \sigma_{xy}^T & \sigma_{yy} \end{pmatrix}, \tag{5.2}$$

where $\sigma_{\mathbf{xx}}$ and $\sigma_{\mathbf{yy}}$ are the familiar 2D beam matrices describing the beam parameters in the horizontal and vertical planes, respectively, and $\sigma_{\mathbf{xy}}$ describes the matrix of the coupling terms (where σ_{xy}^T is simply the transpose of $\sigma_{\mathbf{xy}}$).

This is a valid characterization of the beam even without coupling, in which case the $\sigma_{\mathbf{xy}}$ and $\sigma_{\mathbf{xy}}^{\mathbf{T}}$ terms would simply be zero. If a single element of the beam matrix is nonzero, the xy-coupling and the projections onto the transverse planes will cause an increase of the *observed emittance*. This is sometimes called the *apparent emittance*. When a statistical treatment of the emittance in which xy-coupling is observed is given, it is sometimes called *intrinsic emittance* [26].

Much like the method of solving for the beam emittance in the horizontal and vertical planes by measuring the $\langle x^2 \rangle$ and $\langle y^2 \rangle$ elements, the $\langle xy \rangle$ element must be measured in order to build the $\sigma_{\mathbf{xy}}$ matrix. Since one of the 2×2 matrices in the coupling regime is simply the transpose of the other, there will be focus only on the σ_{xy} matrix. Akin to Eq. (3.19), the transformation of $\langle xy \rangle$ is given as:

$$\sigma_{13} = \langle xy \rangle = R_{11}R_{33}\sigma_{13}^{(0)} + R_{12}R_{33}\sigma_{23}^{(0)} + R_{11}R_{34}\sigma_{14}^{(0)} + R_{12}R_{34}\sigma_{24}^{(0)}, \tag{5.3}$$

where the measurable beam matrix elements are:

$$\sigma_{11} = \sigma_x^2 = \langle x \cdot x \rangle = \langle x^2 \rangle \tag{5.4}$$

$$\sigma_{13} = \sigma_x y^2 = \langle x \cdot y \rangle = \langle xy \rangle \tag{5.5}$$

$$\sigma_{33} = \sigma_y^2 = \langle y \cdot y \rangle = \langle y^2 \rangle \tag{5.6}$$

From this point on, the same procedure as described in the previous chapters will be followed. In the case of the two 2×2 matrices, representing the horizontal and vertical beam matrices $\sigma_{\mathbf{xx}}$ and $\sigma_{\mathbf{yy}}$, n measurements are taken of the $\langle x^2 \rangle$ and $\langle t^2 \rangle$ beam parameters. Likewise, n measurements are taken of the $\langle xy \rangle$ parameter and the equations can be applied in similar form to Eq. (3.20), where $\mathbf{b}$, $\mathbf{A}$, and $\mathbf{x}$ are replaced by:

$$\mathbf{b} \Rightarrow \mathbf{l} = \begin{pmatrix} \sigma_{13s}^{(a)} \\ \sigma_{13s}^{(b)} \\ \vdots \\ \sigma_{13s}^{(n)} \end{pmatrix} \tag{5.7}$$

$$\mathbf{A} \Rightarrow \mathbf{E} = \begin{pmatrix} R_{11}^{(a)} R_{33}^{(a)} & R_{12}^{(a)} R_{33}^{(a)} & R_{11}^{(a)} R_{34}^{(a)} & R_{12}^{(a)} R_{34}^{(a)} \\ R_{11}^{(b)} R_{33}^{(b)} & R_{12}^{(b)} R_{33}^{(b)} & R_{11}^{(b)} R_{34}^{(b)} & R_{12}^{(b)} R_{34}^{(b)} \\ \vdots & \vdots & \vdots & \vdots \\ R_{11}^{(n)} R_{33}^{(n)} & R_{12}^{(n)} R_{33}^{(n)} & R_{11}^{(n)} R_{34}^{nb)} & R_{12}^{(n)} R_{34}^{(n)} \end{pmatrix} \tag{5.8}$$

$$\mathbf{x} \Rightarrow \kappa = \begin{pmatrix} \sigma_{13q} \\ \sigma_{23q} \\ \sigma_{14q} \\ \sigma_{24q} \end{pmatrix} \tag{5.9}$$

As before, the beam matrix elements can be obtained from a least-squares fit and the variances (diagonal elements) and co-variances (off-diagonal elements) are given by the matrix:

$$\mathbf{C} \Rightarrow \mathbf{F} = \left(\mathbf{E^T E}\right)^{-1} \tag{5.10}$$

Combining these results with those from the beam matrices in the horizontal and vertical planes, it is now possible to construct the 4D beam matrix of Eq. (5.1) and, subsequently, the 4D emittance:

$$\epsilon^{4D} = \sqrt{det\left(\sigma^{\mathbf{4D}}\right)} \tag{5.11}$$

CHAPTER 6

PYTHON PROGRAMMING

6.1 Introduction

This research is mainly aimed at developing a tool that can complement an "automated" quad-scan system that was written in PYTHON - a computer language for scientific missions. From the raw data files containing the quad-scan measurements, this tool can quickly calculate various beam parameters including: beam matrices, beam size, geometrical and normalized emittances, and the Courant-Snyder parameters, to name a few. This chapter will detail the quad-scan measurement tool and the beam parameter analysis tool that was developed for this project.

6.2 Quadrupole Scan Procedure at FAST

Quad-scans at FAST beamline are straightforward to perform. Using the ACNET control system, the operator selects a particular quadrupole magnet to perform the scan with and TPM to image the beam with. The magnetic field is controlled by the current administered to the quadrupoles and these current readings are provided by the ACNET console. The operator simply toggles two knobs to either raise or lower the current (it is also possible to enter a specific current setting, in amps, and raise or lower the current to that setting instantly). An equation for the conversion of the quadrupole current to quadrupole field strength is given in Eq. (1.21).

The spot size is viewed as a 2D projection of the horizontal and vertical planes and it is typical to select a pseudo color map that gives the intensity of the beam as shown in Fig. 6.1. A Gaussian fitting function is applied to the centroid of the beam in each plane and the beam size is given in pixels ($1\,pixel = 9.3\,\mu m$).

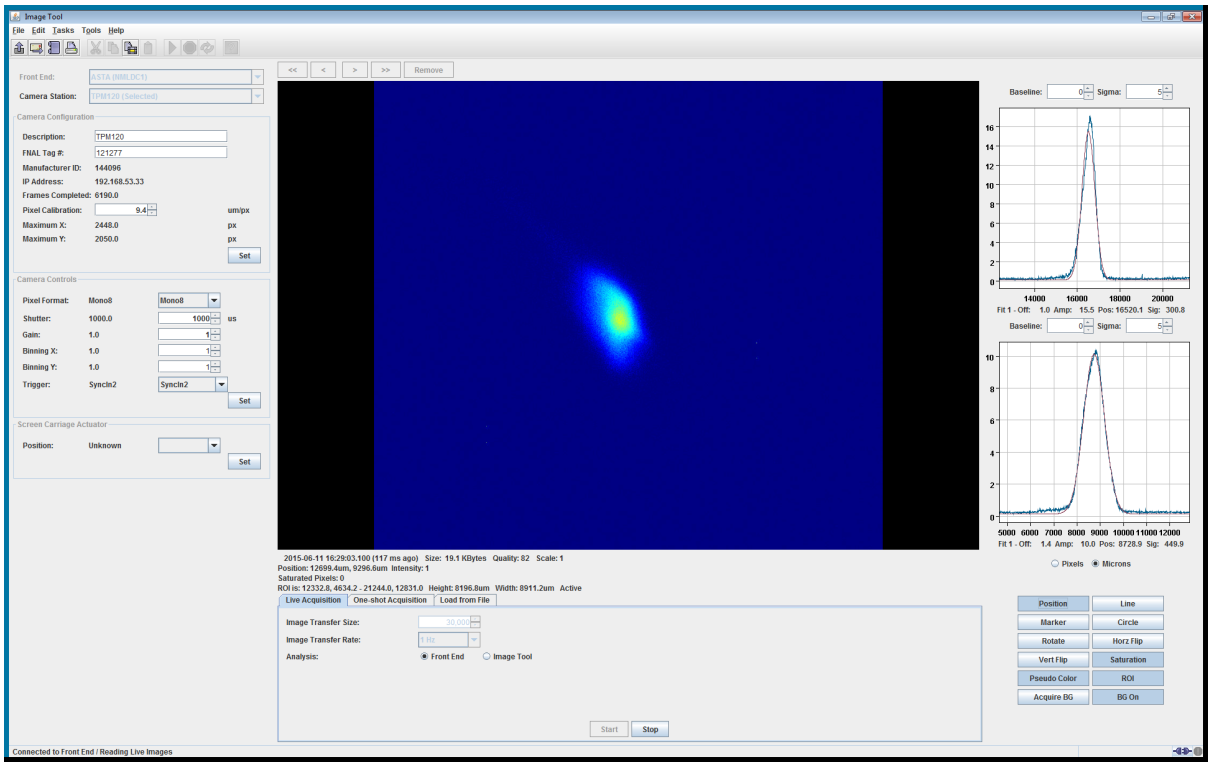

Figure 6.1: 2D projection of the spot size as viewed from a TPM on the ACNET console at FAST. A pseudo color map is being used here to show the beam intensity. The plots on the right show the fitting of the horizontal and vertical beam sizes. For reference, the axes of the imaging area have a width of 8911.2 μm and height of 8196.8 μm.

If the thin lens approximation is used to determine the emittance and Courant-Snyder parameters, the best experimental method is to first find the beam waist, since the emittance is determined by first constructing the beam matrix in Eq. (2.14) and a polynomial fit is applied to the data. Since the polynomial fit is of 2nd order and a plot of the squared beam size as a function of quadrupole field strength is needed to determine the beam matrix elements, the best fit will be one in which the minimum beam size is found.

This will produce a symmetric (or semi-symmetric) parabola with the minimum beam size at the minimum of the parabola and is accomplished by toggling the two quadrupole current switches until a point is found in which both increasing or decreasing the quadrupole current leads to an increase in the spot size. One then scans the quadrupole by selecting a (preferably symmetric) current range on either side of the beam waist and recording the current setting and beam size over the desired range.

6.3 "Automated" Quad-Scan Tool

Prior to the development of a quad-scan tool, an experimenter had to manually toggle the quadrupole current to scan the magnetic field strength k and also manually record the beam size. During the commissioning of the 20 MeV beamline, an "automated" quad-scan tool was developed in PYTHON to decrease the time it took to perform a quad-scan. Originally quad-scans took up to 2 hours and when the preliminary version of the quad-scan tool was implemented at FAST it reduced the experimental time to less than 10 minutes.

During the construction of the 50 MeV beamline,in which the second accelerating cavity was put into place (CC-1), a significant upgrade was made to the "automated" quad-scan system and later implemented during the commissioning of the 50 MeV beamline [27]. The goal of this project was then to develop an emittance and beam parameter calculator to analyze the raw data produced by the quad-scan system.

Some of the new quad-scan tool functions include:

- The ability to record single or multiple beam size measurements per quad current setting.
- Beam size measurements via Gaussian fitting and/or RMS beam size measurements.

- The ability to measure the cross=plane coupling term.
- Saving images of the beam size for each scan point for offline analysis.
- Depending on the desired settings, quad-scans take between 5 - 30 minutes.

A flow chart of the required steps and subsequent output for the quad-scan tool is provided in Fig. 6.3 at the end of this chapter.

There are several user inputs needed before running the quad-scan tool:

1. The quad and TPM used for the quad-scan.
2. The server being used.
3. The number of beam sizes to measure per scan point.
4. The number of data points (k-values) to scan.
5. The scan range. This is determined by first using the ACNET imaging tool to find the minimum beam size or beam waist by toggling the quad current. The desired scan range (the minimum and maximum current settings) must then be entered in the quad-scan tool.

Once the user is finished with the requisite inputs, the tool may be started. During the quad-scan, the system performs the following actions:

1. The laser shutter is enabled, thereby blocking the photocathode laser that shines on the cathode which then disables the electron beam. At this time, the tool acquired an image of the background.
2. Next the shutter is then lifted, restoring beam, and an image of the beam on the screen at the TPM is captured. An image of the beam size with the background subtracted is then saved.

3. Finally, a window appears in the console showing: a pseudo color map of the acquired beam size image, individual plots of the beam size in the transverse planes with a Gaussian fit, printed values of the beam size (σ_x and σ_x) in $pixels$, and finally printed RMS values for $\langle x^2 \rangle$, $\langle y^2 \rangle$, and $\langle xy \rangle$.

A function was built into the quad-scan system that requires the user to accept each image/result before moving on to the next scan point. This is used as a check in the instance that the software or the ACNET console provides a corrupt measurement (for example, if the server crashes then the measurement will be corrupted).

There are then three outputs given by the program: images taken of the beam size for each k-value, a beam parameter log containing various beam parameters settings recorded during the quad-scan (beam energy, bunch charge, etc.), and finally data files containing the k-values and measured beam sizes. For the Gaussian fit, the file will contain three columns of data: the quad current in amps, the horizontal beam size in $pixels$, and the vertical beam size in $pixels$. For the RMS measurements, the file will contain four columns of data: the quad current in amps, $\langle x^2 \rangle$ in $pixels$, $\langle y^2 \rangle$ in $pixels$, and $\langle xy \rangle$ in $pixels$.

6.4 Emittance Calculator

As mentioned, to complement the "automated" quad-scan tool an emittance calculator was developed (also in PYTHON) to process the raw data files and output various estimated beam parameters. The PYTHON-based emittance calculator was programmed with the "thick lens" model and follows the equations for beam matrix formulation, emittance and Courant-Snyder calculation, and error estimation as described in Chapter's 3-5.

The goal was to produce a flexible, user friendly program. The script contains a database of all the quadrupole and TPM locations and will automatically calculate the drift length,

necessary for the relevant equations, based on the input of the assigned quad and TPM names. The naming convention at FAST for quadrupole magnets is "qXXX", where "XXX is a three-digit number (for example: q120) and TPMs are designated "xYYY", where "YYY" is also a three-digit number (for example: x121). The algorithm will also make any necessary conversions such as quad current (in A) to k-values (in m^{-2}), the beam size in $pixels$ to $meters$, etc.

The emittance calculator will also use the appropriate quadrupole matrix (focusing or defocusing in the respective planes) based on the sign of the quadrupole current, and in-turn the k-value. Depending on the number of beam size measurements recorded per scan point, the algorithm will assign a statistical error to the beam size measurements or a systematic error of 20 μm (the resolution limit of the CCD cameras in the TPM).

A flow chart of the procedure for using the emittance calculator can be found in Fig. 6.4 at the end of this chapter.

Prior to running the PYTHON script, the user must enter three inputs:

1. The file path/directory to where the output data file from the quad-scan tool is saved.

2. The error to be used:

   - If statistical error is to be used, then the user must set "Navg" equal to the number of beam size measurements per scan point (k-value) that was implemented in the quad-scan tool.

   - If systematic error is used, then "Navg" is set equal to one (the default) and the algorithm will apply the 20 μm resolution limit of the CCD camera.

3. The user must enable/disable the RMS calculations by commenting/uncommenting a line of the code.

The last input from the list above, whether or not RMS measurements are read in from the quad-scan tool, were a last-minute adjustment during the quad-scan experiments. There were time constraints on the experiments during the commissioning phase and, for the sake of time, the RMS measurement function was disable in the quad-scan tool. Using full functionality, including both Gaussian fitting and RMS measurements, the quad-scans took approximately 30 minutes. It was discovered that the RMS calculations from the script took the most time to complete and so it was decided to turn this function off. Using only Gaussian fits, the quad-scans took 5-10 minutes. However, since images for each scan point are saved, off-line RMS analysis is possible. The emittance calculator expects either three columns of data for the Gaussian fit or four columns of data for the RMS measurements, so there is a line of code in the emittance calculator that must be turned off if the Guassian fit is used (by "commenting out" the line) or turned on for RMS calculations (by "uncommenting" the line of code).

After preparation has been completed, the emittance calculator tool may be started. Immediately upon starting the script, the user is given three prompts to enter: the beam energy in MeV and the quad name and TPM name as described in the previous section.

The emittance calculator will then print the results in the PYTHON shell, print a text file containing the results, and display a plot of the beam size (in mm) versus the quadrupole field strength (in m^{-2}) complete with fits in each transverse plane and error bars for the beam sizes. The full list of estimated parameters from the output include:

- Drift length (m).
- Beam size (m) at the entrance of the quad in both planes $\pm$ the error.
- 4D beam matrix.
- Geometrical emittance ($mm \cdot mrad$) in both planes $\pm$ the error.

- Normalized emittance ($mm \cdot mrad$) in both planes $\pm$ the error.
- 4D emittance.
- Courant-Snyder parameters (Twiss parameters) in both planes $\pm$ the error.

Figure 6.2 shows an example of the plot of the beam size versus quadrupole k-value produced by the program.

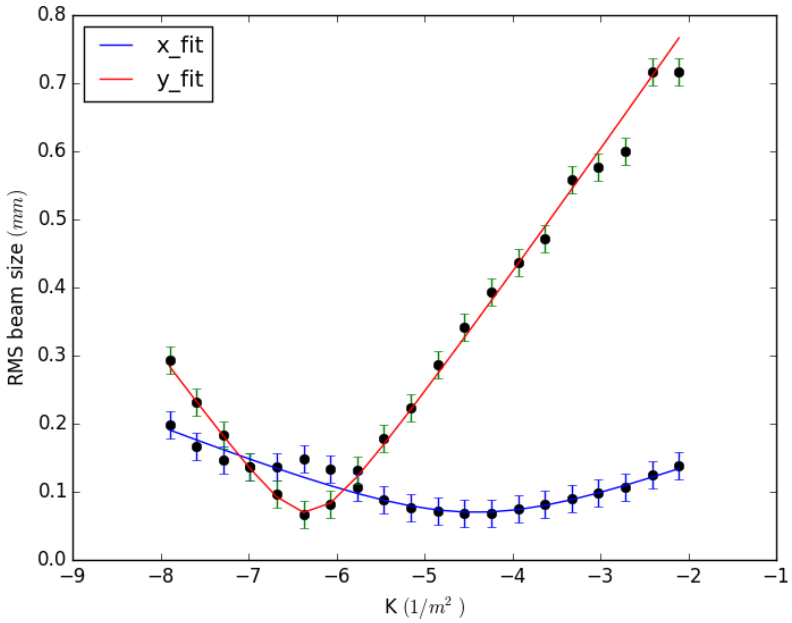

Figure 6.2: An example of the beam size vs. k from the emittance calculator. The geometrical emittance, along with the associated error, is printed at the top of the plot.

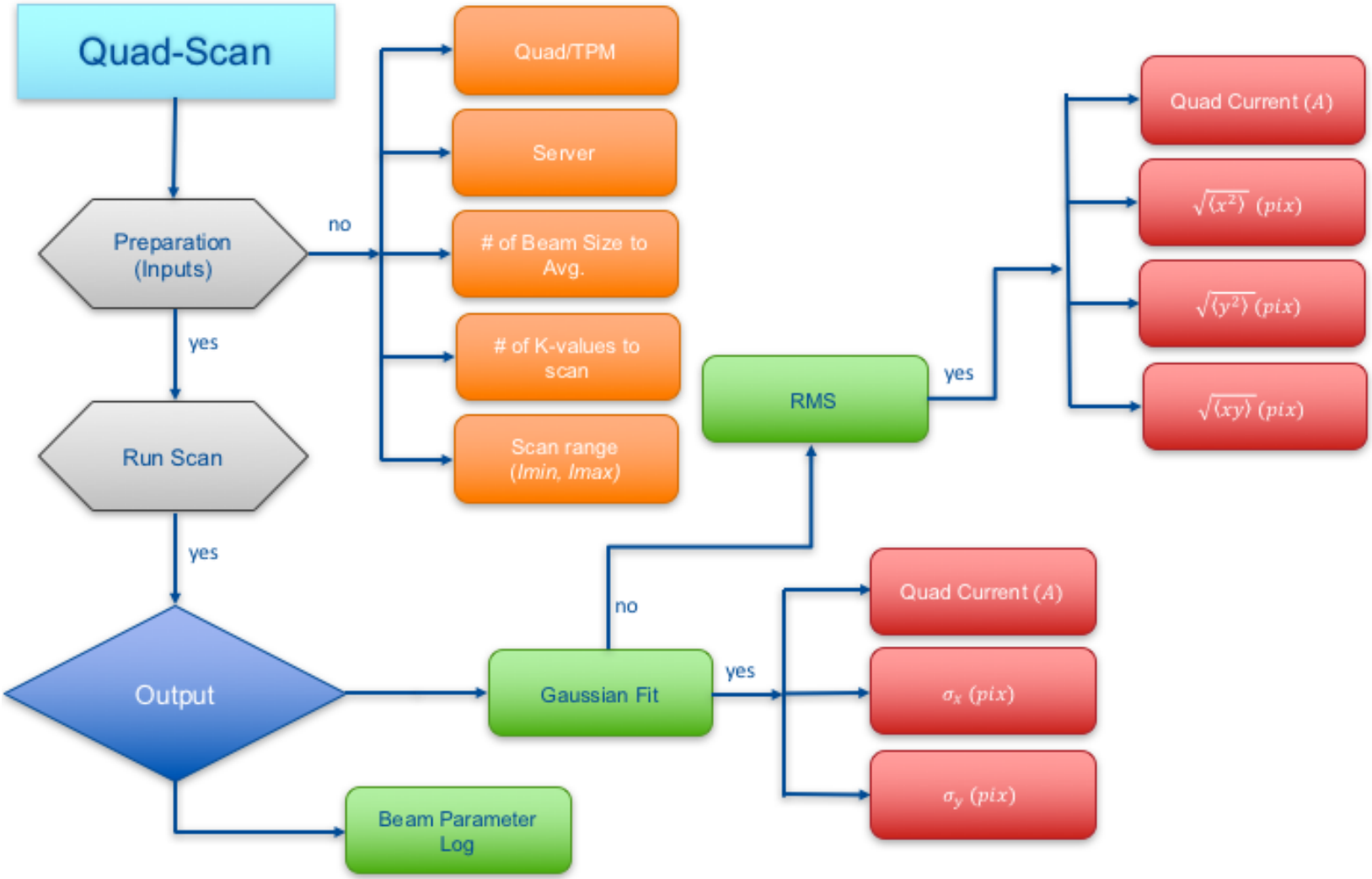

Figure 6.3: A big figure that needs to go sideways.

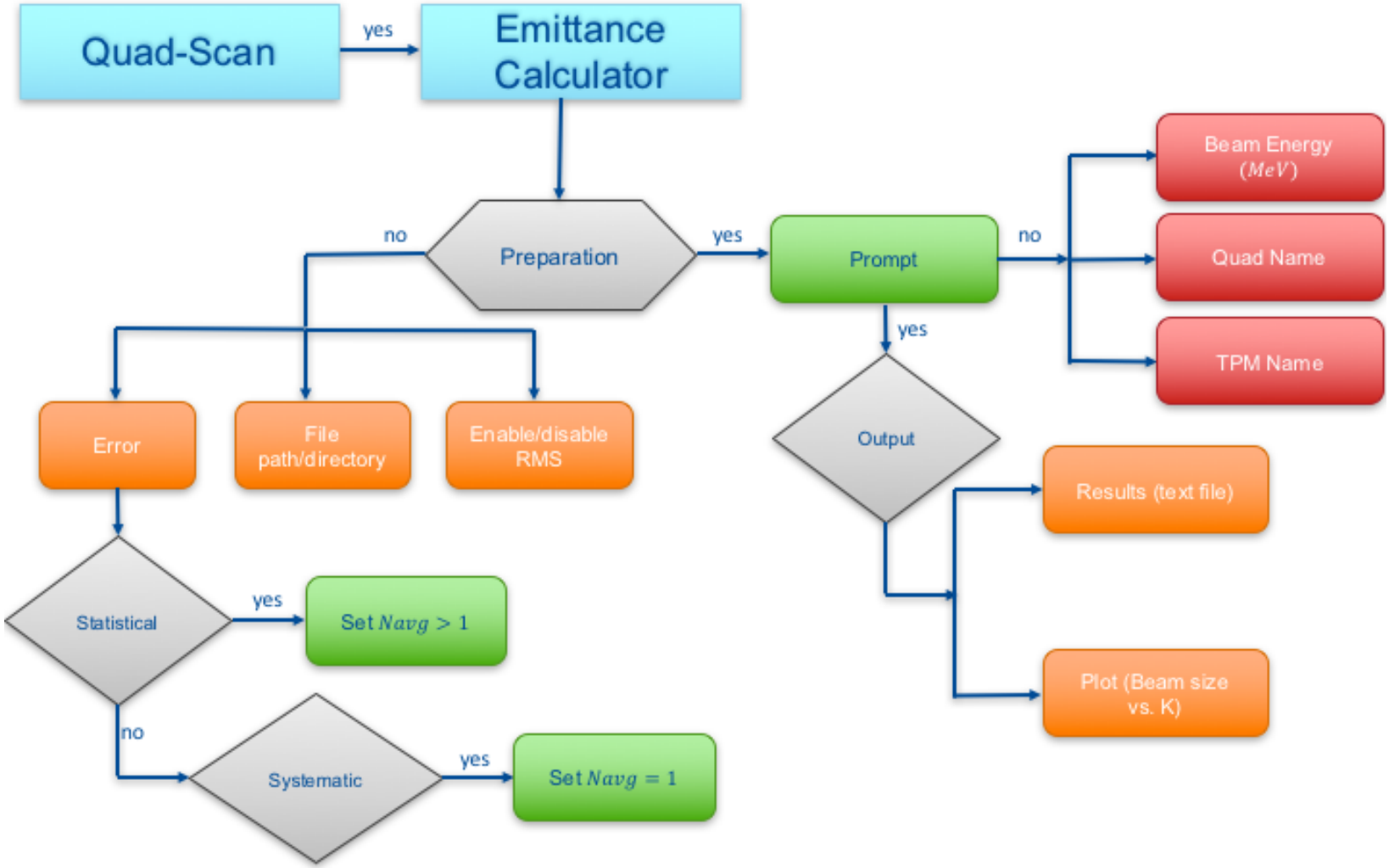

Figure 6.4: A big figure that needs to go sideways.

CHAPTER 7

FAST EXPERIMENTAL RESULTS AND ANALYSIS

7.1 Introduction

This chapter will provide experimental results collected at FAST beamline using the PYTHON-based automated quad-scan and emittance calculator tools. The plot in Fig. 7.1 shows the predicted transverse emittance in the horizontal (black) and vertical (red) planes via ELEGANT simulation for 25 MeV electrons [28]. This simulation code predicted $\sim$ 1 $mm \cdot mrad$ horizontal emittance and $\sim$ 1.5 $mm \cdot mrad$ vertical emittance. In May 2016 a 50 MeV beam was achieved with the addition of the second capture cavity (CC-1). ELEGANT simulation with the FAST beamline lattice and the new capture cavity yielded a normalized emittance of $\sim$ 2 $mm \cdot mrad$. In this chapter discussion of some simulation results for matching with the PYTHON algorithm, comparison of the PYTHON emittance calculator with one written in ELEGANT, and finally some experimental results from quadrupole scans collected during the 50 MeV beamline commissioning will be given.

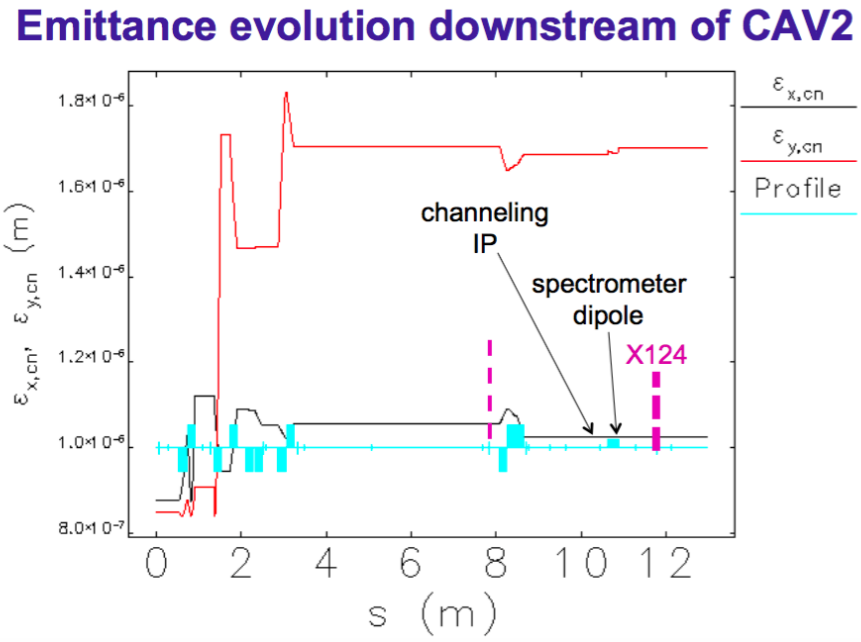

Figure 7.1: ELEGANT simulation of the transverse emittance in the low-energy beamline at FAST between the second capture cavity and the low-energy absorber. The beam parameters in this simulation include a beam energy of 25 MeV and bunch charge of 250 pC [28].

7.2 ELEGANT Simulation

To benchmark the PYTHON scripts for emittance calculation, several quadrupole scans were simulated with ELEGANT particle tracking simulation [29]. Tables 7.1 and 7.2 show results from two of these simulations. Using a FAST lattice file, quad-scans were simulated with two different quadrupoles at two different TPMS. After performing the simulation, the k-values and beam sizes were arranged in a data file for processing with PYTHON to test the algorithm.

Table 7.1 shows simulation results with quad q106 at the TPM x109, with a drift length of $\approx 1.3\,m$ between them and a beam energy of $50\,MeV$. As shown from the simulated geometrical emittances in the transverse planes and the calculated emittances from PYTHON, there is less than a $< 5\%$ difference. Likewise, Table 7.2 shows the same simulation parameters only with q108 and x111 this time (drift length $= \approx 1.2\,m$) at $50\,MeV$. The error in this case was $< 3\%$.

The likely source of the small discrepancy is the systematic error that was applied to the data in PYTHON, but not in ELEGANT. ELEGANT assumed no error, however the emittance calculator must accept some form of statistical or systematic error in order to function and so the camera resolution limitation (the systematic error) was applied to all of the measured beam sizes provided by the ELEGANT file.

Table 7.1: Table showing geometrical emittance calculated by quad-scans with ELEGANT and PYTHON using quadrupole q106 and TPM x109 (drift length: $1.3\,m$, Beam energy: $50\,MeV$).

	ELEGANT	**PYTHON**	**% Difference**
ϵ_{xg}	$1.00 \times 10^{-8}\,m \cdot rad$	$9.56 \times 10^{-9}\,m \cdot rad$	$< 5\%$
ϵ_{y_g}	$1.50 \times 10^{-8}\,m \cdot rad$	$1.43 \times 10^{-8}\,m \cdot rad$	$< 5\%$

Table 7.2: Table showing geometrical emittance calculated by quad-scans with ELEGANT and PYTHON using quadrupole q108 and TPM x111 (drift length: $1.3\,m$, Beam energy: $50\,MeV$).

	ELEGANT	**PYTHON**	**% Difference**
ϵ_{xg}	$1.50 \times 10^{-8}\,m \cdot rad$	$1.46 \times 10^{-8}\,m \cdot rad$	$< 3\%$
ϵ_{y_g}	$1.75 \times 10^{-8}\,m \cdot rad$	$1.70 \times 10^{-8}\,m \cdot rad$	$< 3\%$

7.3 Experimental Results

As this paper is being written, the $50\,MeV$ beamline is being commissioned at FAST. For the first time, the PYTHON scripts were implemented in the control room and the emittance calculator was employed in an experimental setting with the use of the updated quad-scan code. Herein the test results are presented with measured data.

7.3.1 Preliminary Quad-Scans

The first quad-scans were performed with Q110 at X111. The goal was to begin measuring emittance shortly after the capture cavities. The experiment was performed by running codes that centered the beam through the two capture cavities and the quadrupoles. It was observed that through quadrupole focusing, steering of the beam was occurring due to misalignment. Incrementally, alignments were made by accurately steering the beam through the center of the quads with the support of small dipole magnets called "corrector magnets". The following figure and table shows a typical early quad-scan results with a beam energy of 41.1 MeV.

Table 7.3: Table showing early experimental results from a quad-scan with q110/x111 (drift length = $0.421\,m$).

Plane	**Beam energy** (MeV)	**Beam size** (mm)	ϵ_n $(mm \cdot mrad)$	β (m)	α
x	41.1	$3.11 \pm 9.78 \times 10^{-3}$	$80.9 \pm 1.54 \times 10^{-3}$	$7.13 \pm 1.45 \times 10^{-4}$	$9.73 \pm 1.99 \times 10^{-4}$
y	41.1	$3.14 \pm 1.03 \times 10^{-2}$	$101 \pm 1.72 \times 10^{-3}$	$5.72 \pm 1.06 \times 10^{-4}$	$7.94 \pm 1.45 \times 10^{-4}$

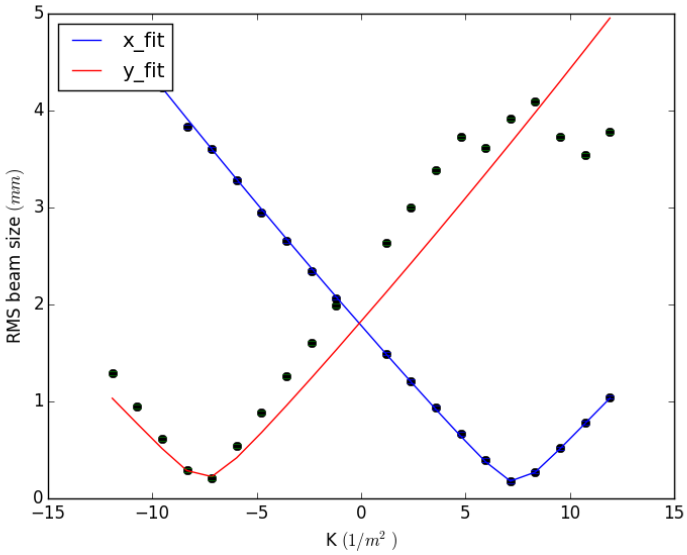

Figure 7.2: Beam size vs. K for Q110/X111 showing both transverse planes. The blue line represents the horizontal (x) data and the red represents the vertical (y) data.

It is clear from the Fig. 7.2 that the fits are bad. This happened on many occasions as the minimum beam size in each plane occurred at quite different quadrupole field strengths at times. For this reason, after finding the minimum beam size in each plane, scans were typically performed over the beam waist range individually in each plane. An explicit example of this can be seen in Figures 7.3 and 7.4. Here, the quad-scan was performed twice more with the same settings, only the quadrupole was scanned over a narrowed range around the minimum in each plane for a better fit.

In these plots, one can see that the fits in their respective planes are improved. From the first few experiments-on, it was decided to scan individual planes to achieve the best results. From the normalized emittance results the emittance was far larger than the simulated results of $2\,mm \cdot mrad$ normalized emittance. For scans up to 35 k-values, the time it took to perform a quad-scan was around 5 minutes. The emittances measured in the early tests ranged from $12 - 15\,mm \cdot mrad$ (normalized), as shown in Fig. 7.5.

Table 7.4: Table showing early experimental results from a quad-scan with q110/x111 (drift length = 0.421 m).

Plane	**Beam energy** (MeV)	**Beam size** (mm)	ϵ_n $(mm \cdot mrad)$	β (m)	α
x	41.1	$3.16 \pm 1.23 \times 10^{-2}$	$81.2 \pm 1.58 \times 10^{-3}$	$7.32 \pm 1.69 \times 10^{-4}$	$10.0 \pm 2.35 \times 10^{-4}$

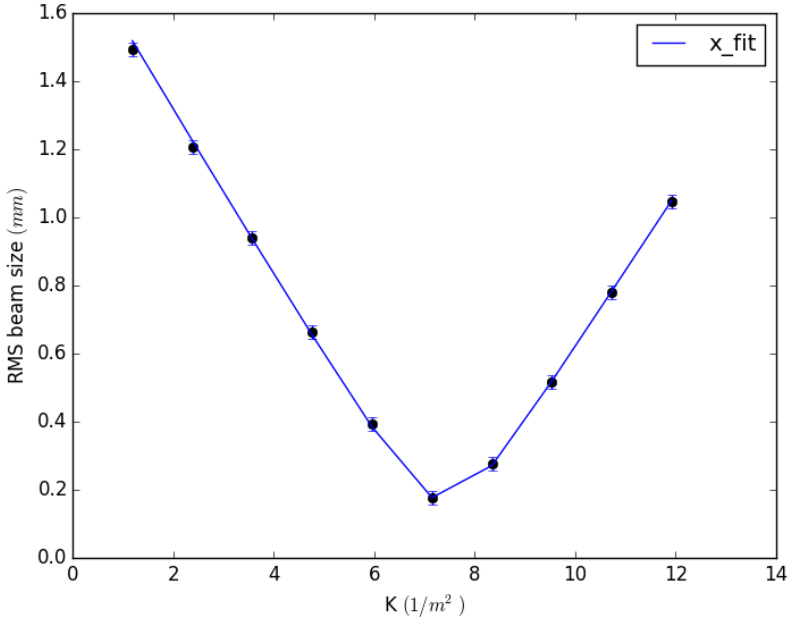

Figure 7.3: Beam size vs. K for Q110/X111 showing only the horizontal plane (x).

Table 7.5: Table showing early experimental results from a quad-scan with q110/x111 (drift length = 0.421 m).

Plane	**Beam energy** (MeV)	**Beam size** (mm)	ϵ_n $(mm \cdot mrad)$	β (m)	α
y	41.1	$4.09 \pm 1.59 \times 10^{-2}$	$102 \pm 2.97 \times 10^{-3}$	$13.4 \pm 4.57 \times 10^{-4}$	$9.47 \pm 3.17 \times 10^{-4}$

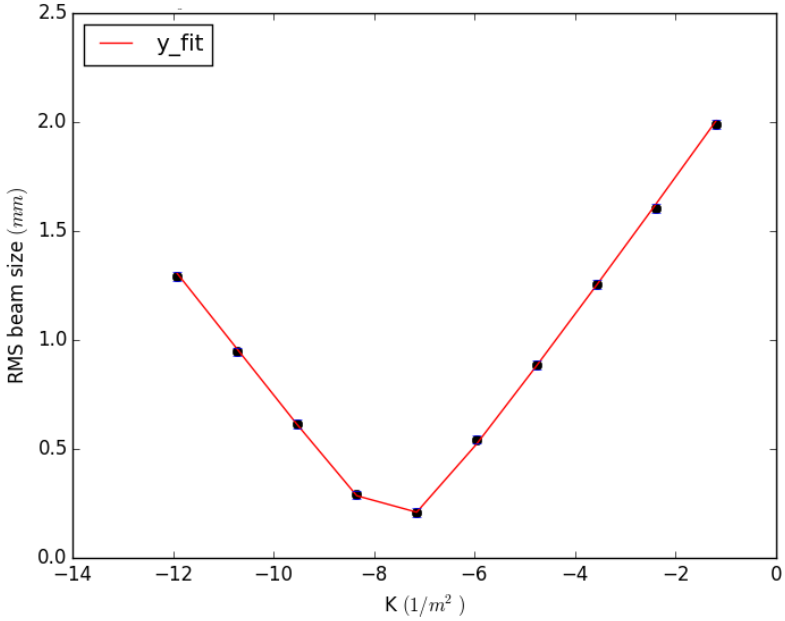

Figure 7.4: Beam size vs. K for Q110/X111 showing only the vertical plane (y).

Table 7.6: Table showing early experimental results from a quad-scan with q110/x111 (drift length = 0.421 m) with lower emittance.

Plane	**Beam energy** (MeV)	**Beam size** (mm)	ϵ_n $(mm \cdot mrad)$	β (m)	α
x	41.1	$0.543 \pm 1.97 \times 10^{-3}$	$11.7 \pm 9.23 \times 10^{-5}$	$2.04 \pm 2.44 \times 10^{-5}$	$5.63 \pm 6.49 \times 10^{-5}$
y	41.1	$0.612 \pm 2.11 \times 10^{-3}$	$17.5 \pm 1.17 \times 10^{-4}$	$2.15 \pm 2.72 \times 10^{-5}$	$1.69 \pm 2.56 \times 10^{-5}$

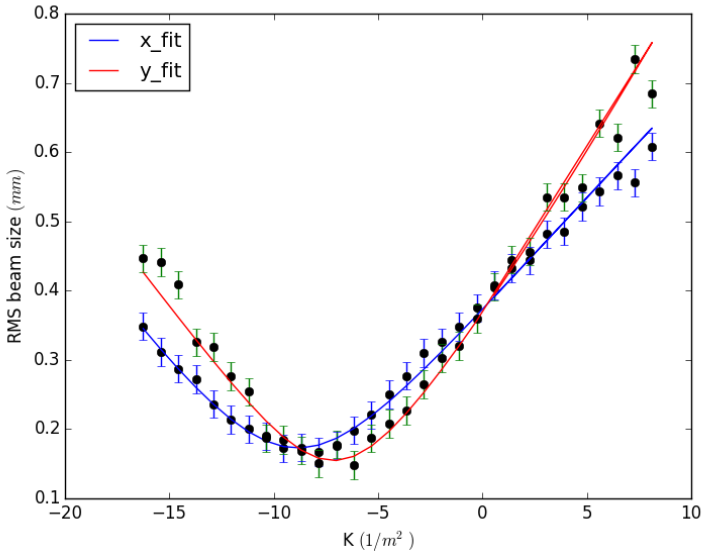

Figure 7.5: Beam size vs. K for Q110/X111 showing both transverse planes with lower emittance. The blue line represents the horizontal (x) data and the red represents the vertical (y) data.

7.3.2 Main Solenoid Scans

A quick beam phase space evaluation tool is developed in the purpose of integrating the automated quad-scan program in the ACNET console at FAST. Deploying the tool in the beamline control system was successfully established with measurement of emittances by the quad-scan method. Since the emittance was, however, still larger than predicted by simulations (by a factor of 3 or 4), a solenoid condition upstream CC1 has been optimized with the quad-scan beam emittance measurement. There are two solenoids immediately after the gun a main solenoid and a bucking solenoid. The nominal settings for the main and bucking solenoids since the 20 MeV beamline had been commissioned was $290 - 295\,A$ and $70 - 75\,A$, respectively. Quad-scans were performed over the course of two days to see if it was possible to optimize the solenoids for the lowest emittance at the current settings.

After further tuning of the beamline, q108 and x111 were used to first scan the main solenoid and later, after finding the optimum setting, to scan the bucking solenoid. Figures 7.6 and 7.7 show plots of the results from the main solenoid scan. Beginning with 292 A, the main solenoid was scanned in 5 A increments up to 327 A. It was discovered that the optimum solenoid setting was around 312 A, dropping the emittance by a factor of 3, or $5 - 7\,mm \cdot mrad$. Figure 7.7 shows the same plot as calculated by an ELEGANT code for comparison, showing close agreement. More studies are needed to uncover the discrepancies between the two codes. One such discrepancy, which was previously an issue when comparing to ELEGANT, was error analysis. The only source of error considered for these scans in PYTHON was the systematic error coming from the camera resolution limit of $20\,\mu m$. There are indeed error bars being displayed in Fig. 7.6, but they are four orders of magnitude smaller than the emittance, which are therefore unseen unless each data point is zoomed in on.

These quad-scan/solenoid scans were performed over the course of two days. During the first day (6/3/16), quad-scan was performed with $295 - 317\ A$ of solenoid current. The next day, the scan was resumed, but backtracked to the $312\ A$ main solenoid setting (the optimum setting). Prior to performing the first quad-scan at $312\ A$, the beamline was reset with the same parameters as the previous day. As shown in Figures 7.6 and 7.7, these settings seemed optimum as the beam appeared centered and the emittances were replicable for the two repeated solenoid settings of $312\ A$ and $317\ A$.

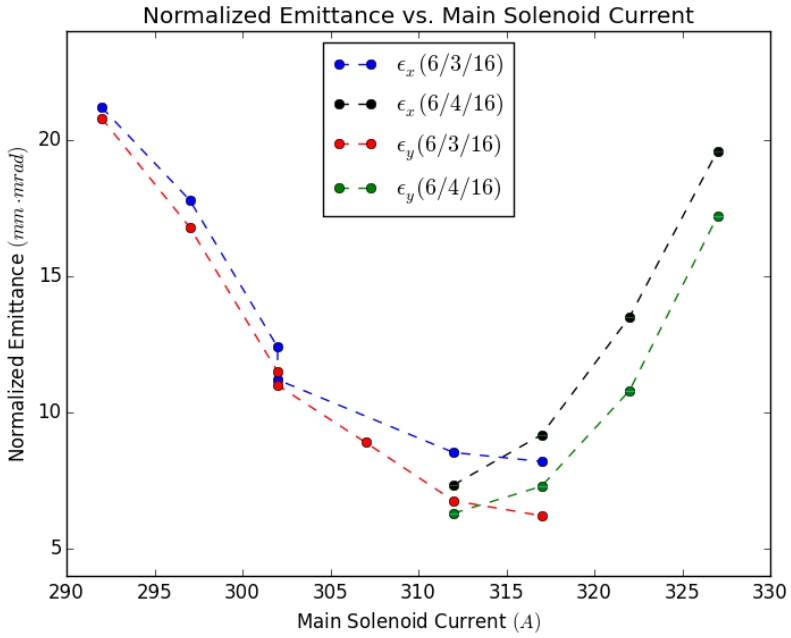

Figure 7.6: Plot of emittance as a function of the main solenoid current as calculated by PYTHON. Scans were performed on two separate days: blue/black refer to the horizontal plane and red/green refer to the vertical plane. The beam energy was 40 MeV and the bunch charge was 200 pC.

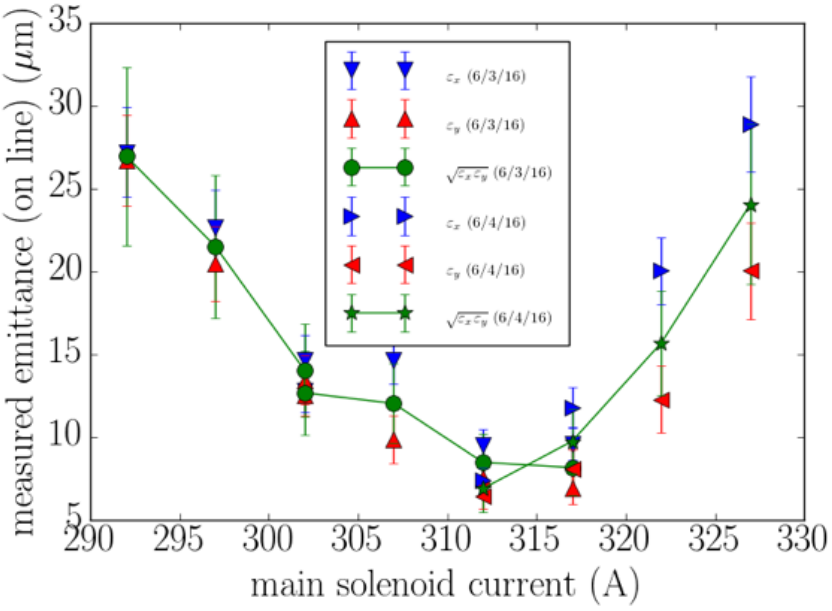

Figure 7.7: Plot of the emittance as a function of the main solenoid current as calculated by ELEGANT. This is the same data as presented in Fig. 7.6, only using ELEGANT to compute the emittance.

7.3.3 Bucking Solenoid Scans

Following the main solenoid scans, attempts at lowering the emittance were continued and the same procedure was applied to the bucking solenoid. The main solenoid was set to the optimal setting (312 A) and the bucking solenoid was scanned from $20 - 140$ A in 20 A increments. Figures 7.8 and 7.9 display these results, again with both PYTHON and ELEGANT, respectively. From the analyzed data it was concluded that the nominal setting of $70 - 75$ A was indeed the optimal setting for low emittance.

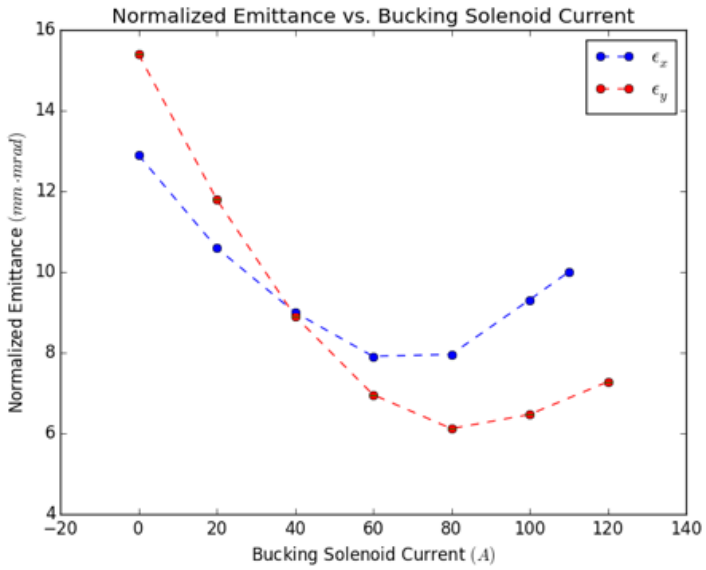

Figure 7.8: Plot of emittance as a function of the bucking solenoid current as calculated by PYTHON. Scans were performed on two separate days: blue/black refer to the horizontal plane and red/green refer to the vertical plane. The beam energy was 40 MeV and the bunch charge was 200 pC.

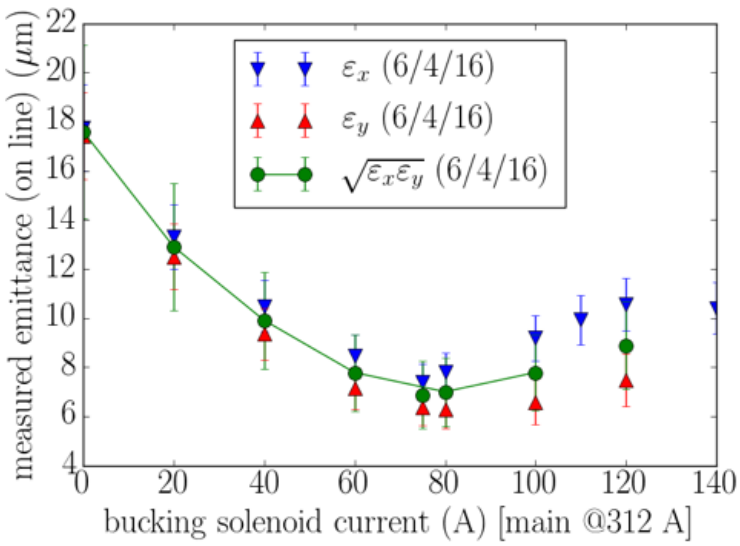

Figure 7.9: Plot of the emittance as a function of the bucking solenoid current as calculated by ELEGANT. This is the same data as presented in Fig. 7.8, only using ELEGANT to compute the emittance.

7.3.4 Emittance as a Function of Bunch Charge

Studying emittance as a function of bunch charge was also of interest as the various planned experiments will not necessarily use the same charge throughout. Knowing the optimum main solenoid setting was $\approx$ 310 A, quad-scans as a function of both the bunch charge and main solenoid setting were performed as shown in Fig. 7.10. The solenoid was scanned over 295 A, 310 A, and 325 A for 100 pC and 100 bunch charge. As expected, the emittance was lower at lower charge. At the optimum range, the emittance in x decreased by a factor of 2 and in y it decreased by 1 $mm \cdot mrad$.

These quad-scans were performed with a beam energy of 42.3 MeV and 50 bunches in the macro-pulse, again with q108 at x111. It was noticed from the individual quad-scans that some coupling was occurring and the fits began to degrade, particular in the horizontal

plane. As mentioned previously, the normalized emittance from simulation was calculated to be $\approx 2mm{\cdot}mrad$, of which the experimental results were a factor of 3 larger. Possible sources of this larger emittance could be perceived emittance growth due to coupling induced by the laser (since only Gaussian fits were used) or possibly instabilities in the capture cavities.

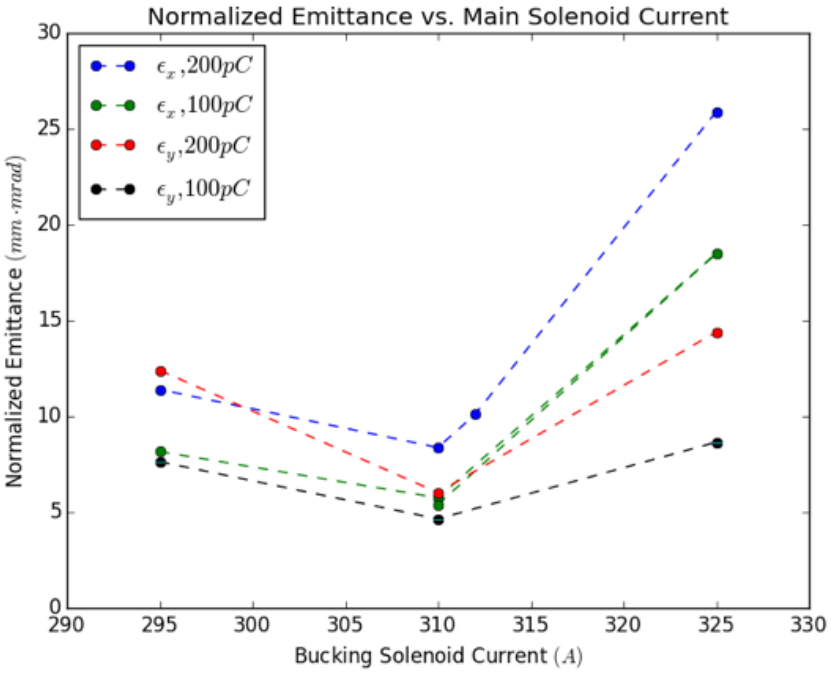

Figure 7.10: Plot of the emittance as a function the main solenoid current and bunch charge.

7.3.5 Emittance at the Goniometer

A goniometer has been installed near the end of the low-energy beamline. One of the planned experiments at FAST is a crystal channeling radiation experiment. There is a crystal within the goniometer and for this experiment a small emittance is needed $\approx 1\,mm \cdot mrad$. It was therefore necessary to measure the emittance at a location near the goniometer to assure the accelerator was capable of achieving the required emittance.

Conveniently, there exists a quadrupole and TPM in the low energy beamline near the goniometer: q120 and x121. It should be noted that throughout the experiments since the upgrade to 50 MeV, OTR screens were used rather than YAG screens (both of which are found in some of the TPMs). This was due to concern that at these energies a YAG screen may cause saturation within the camera when measuring the beam size. At x121, however, the OTR screen faces 90° from the beam path and so the test was limited to use only a YAG screen at this location. It was intended to lower the charge, and thus the emittance, and so such low charges should not have adverse effects on the beam measurement. Reducing the bunch charge to 50 pC and 50 bunches, the emittance was measured to be $\approx 1\, mm \cdot mrad$ in x, but $\approx 5\, mm \cdot mrad$ as shown in figures 7.11 - 7.13. The fitting was again of poor quality at these low charges. When examining the data from this scan in the individual planes, one can see that the poor fits are likely yielding inaccurate results.

Table 7.7: Table showing experimental results from a quad-scan with q120/x121 (drift length = 1.05 m) in both planes. The bunch charge was 50 pC and the beam energy was 42.3 MeV.

Plane	**Beam energy** (MeV)	**Beam size** (mm)	ϵ_n ($mm \cdot mrad$)	β (m)	α
x	42.3	$0.287 \pm 1.26 \times 10^{-3}$	$1.31 \pm 1.20 \times 10^{-5}$	$5.30 \pm 8.38 \times 10^{-5}$	$7.64 \pm 1.24 \times 10^{-4}$
y	42.3	$0.977 \pm 3.26 \times 10^{-3}$	$5.05 \pm 6.98 \times 10^{-5}$	$15.8 \pm 2.63 \times 10^{-4}$	$-2.35 \pm 4.07 \times 10^{-5}$

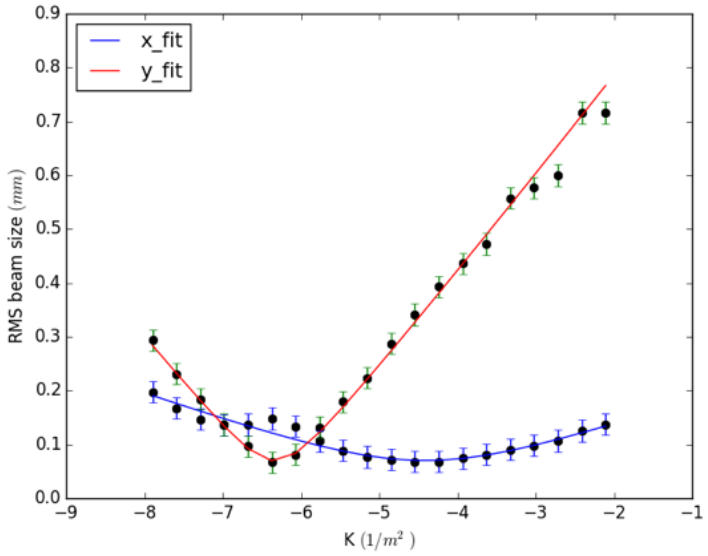

Figure 7.11: Quad-scan results from q120 at x121 with 50 pC bunch charge and 42.3 MeV in both planes.

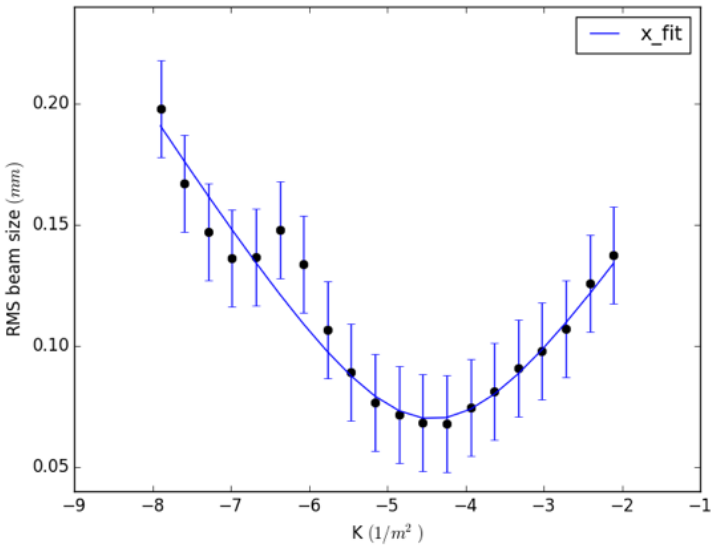

Figure 7.12: Quad-scan results from q120 at x121 with 50 pC bunch charge and 42.3 MeV in the horizontal.

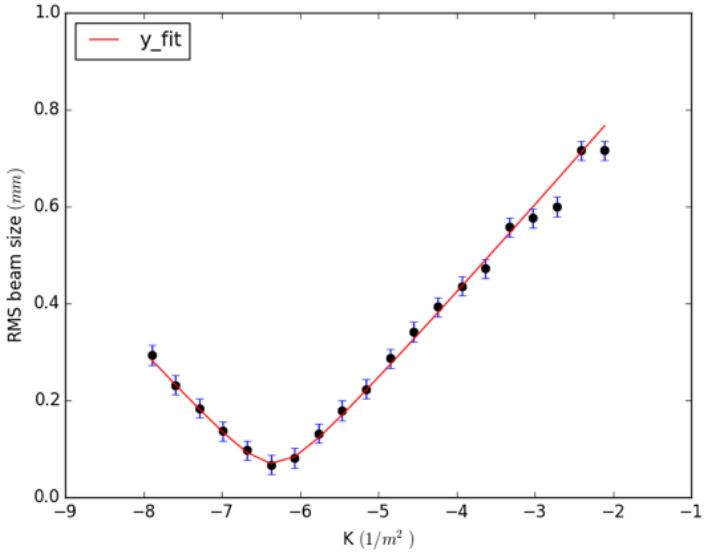

Figure 7.13: Quad-scan results from q120 at x121 with 50 pC bunch charge and 42.3 MeV in the vertical.

CHAPTER 8

SUMMARY AND CONCLUSION

The goal of this research project was to study the quadrupole scan technique for transverse emittance measurements, with a primary focus in delivering an automated quad-scan tool and emittance calculator. Quad-scans are a simple, well understood experimental technique and beam emittance is essential for characterizing a high-quality beam.

Beginning with the thin lens model, the technique for calculating the transverse emittance and Courant-Snyder parameters has been described: by varying a quadrupole magnet and measuring the beam size, it is possible to calculate the beam emittance by plotting the squared beam size versus quadrupole field strength and applying a 2nd-order polynomial fit. The coefficients given by this fit can be used to calculate the emittance as described in Chapter 3.

For a more accurate measurement of the emittance an exact linear model was implemented, the thick lens model. Details of the updated "automated" quad-scan script was also detailed. This tool allows the user to measure the beam size as a function of the quadrupole field strength via Gaussian fits. For a true statistical analysis, the updated quad-scan can also measure the RMS beam size in the transverse planes as well as the coupling term, which is necessary to accurately describe the beam emittance. Should coupling exist, the emittance can appear larger when using Gaussian fits from the 2D projections onto the CCD camera.

To complement the quad-scan system, this project focused on developing a flexible thick lens emittance calculator, also written in PYTHON, giving the user the ability to quickly analyze the raw data file produced from the quad-scan tool. This calculator can analyze both Gaussian and RMS beam sizes, as well has analyzing statistical and/or systematic errors of

the measured beam size and subsequently propagating these errors onto the beam matrix, emittance, and Courant-Snyder parameters via the χ^2/least-squares method.

Following simulations to benchmark the algorithm from the code, the emittance calculator was implemented in an experimental setting in the ACNET control at Fermilabs FAST accelerator R&D facility during the commissioning of the 50 MeV low-energy beamline. By tuning the beam via steering corrections through the capture cavities and quadrupoles, a 5 $mm \cdot mrad$ emittance measurement in the transverse planes was achieved (a factor of 3 smaller than original measurements prior to tuning). Studies involving scanning the main solenoid and bucking solenoid to optimize the emittance were successfully performed. Upon optimization of the beamline and solenoids, measurements of the emittance as a function of the solenoid settings and bunch charge were analyzed. In preparation for the addition of crystal channeling radiation experiments, emittance measurements were taken close to the entrance of the goniometer at low charge to ensure transverse emittance was achievable.

There are several tasks to be performed in the near-future. RMS analysis for statistical treatment is needed for off-line analysis of the current data. Also, the discrepancies between the simulation results and emittance calculations need to be inspected (although the difference may arise from the systematic error implemented in PYTHON).

The simulated lattice yielded 2 $mm \cdot mrad$ normalized emittance at 50 MeV and 00pC, yet the lowest emittance calculated from these settings yielded a normalized emittance of 5 $mm \cdot mrad$. Space charge, the Coulomb repulsive force from the like charges in the beam, might be one factor in this larger emittance. If the space charge force is significant, then it may combat the focusing effects of the quadrupole magnets. Another non-linear effect that may increase the emittance may be chromaticity. The charged particles within the bunch could have a large momentum spread and, if so, the particles will deflect according to their energy and so chromatic effects in the quads may also cause an increase in emittance. These effects have not yet been considered in the quad-scan experiments and thick lens

emittance calculations. Also, analyzing the recently performed quad-scans with a statistical RMS analysis my show that previous estimates of the emittance have been over-estimated if cross-plane coupling exists between the transverse planes.

The PYTHON-based emittance calculator developed during this project has been benchmarked with ELEGANT simulations to confirm the accuracy of the algorithm. This tool has also been field tested under experimental conditions in the ACNET console at Fermilab's FAST facility. Designed with ease-of-use to the user, this flexible PYTHON script quickly delivers results with minimal input and completely complements the advanced "automated" quad-scan tool.

REFERENCES

[1] P. M. Lapostolle, "Possible Emittance Increase Through Filamentation Due to Space Charge in Continuous Beams",*IEEE Trans. Nucl. Sci.* 18 (3) (1971) 1101.

[2] `http://www.python.org`

[3] A. Valishev, "Introduction to IOTA and Injectors", *Focused Workshop on Scientific Opportunities in IOTA*, Fermilab, April 28-29, 2015.

[4] `http://fast.fnal.gov`

[5] D. J. Crawford, et. al., "First Beam and High-Gradient Cryomodule Commissioning Results of the Advanced Superconducting Test Accelerator at Fermilab", *6th International Particle Accelerator Conference*, Richmond, VA., May 3-8, 2015.

[6] D. A. Edwards, M. J. Syphers, *An Introduction to the Physics of High Energy Accelerators*, Wiley-VCH, 2004.

[7] `http://www.linearcollider.org/ILC`

[8] `https://en.wikipedia.org/wiki/Solenoid`

[9] V. Kumar, "Understanding the Focusing of Charged Particle Beams in a Solenoid Magnetic Field", *Am. J. Phys.* 77, 737 (2009).

[10] H. F. Kisoglu, M. Yilmaz, "Beam Dynamical Evolutions in a Solenoid Channel: A Review", *European International Journal of Science and Technology* 27, (2014), 157-164.

[11] J. Holmes, S. Henderson, Y. Zhang, Lecture 2 "Magnetic Fields and Magnetic Design", United States Particle Accelerator School, Vanderbilt, 2009.

[12] O. Chamberlin. "Optics of High-Energy Beams", *Annual Review of Nuclear Science* Vol. 10: 161-192 (December 1960).

[13] `https://www-bd.fnal.gov/controls/acnet.html`

[14] `http://beamdocs.fnal.gov/AD/DocDB/0042/004212/005/ASTA_technical_description.pdf`

[15] J. Buon, "Beam Phase Space and Emittance", Laboratoire de lAccelerateur Lineaire, Orsay, France.

[16] F. Lohl, "Measurements of the Transverse Emittance at VUV-FE", *Diploma Thesis*. DESY-THESIS 2005-014, TESLA-FEL 2005-03, Hamburg, July 2005.

[17] U. Raich, "Emittance Measurements", *Accelerator Beam Diagnostics*, United States Particle Accelerator School, University of New Mexico, Albuquerque, NM. June 23-26, 2009.

[18] H. Wiedemann, *Particle Accelerator Physics*. 3rd Ed. Springer, 2007.

[19] S. Skelton, "Multi-Quadrupole Scan for Emittance Determination at PITZ", *Summer Student Program 2007*, DESY Zeuthen, Vienna University of Technology, 2007.

[20] J. Rudolph, "Slice-Emittance Measurement Techniques", Helmholtz Zentrum Berlin.

[21] G. Strang, *Introduction to Linear Algebra*, 4th Ed., Wellesley Cambridge Press, February 10, 2009.

[22] `http://www.docs.scipy.org`

[23] J. R. Taylor, *An Introduction to Error Analysis*. 2nd Ed., University Science Books, 1997.

[24] P. Tenenbaum, "Emittance Measurements in CTF 2 Drive Beam", *CLIC Note 326*, CERN European Laboratory for Particle Physics, 11.02.97.

[25] J. Rees, L. Rivkin, "On Measuring Emittances and Sigma Matrices", *SLAC-PUB-3305*, SLAC/AP-18. March, 1984.

[26] E. Prat, M. Aiba, "Four-Dimensional Transverse Beam Matrix Measurement Using the Multiple-Quadrupole Scan Technique", *Physical Review Special Topics Accelerators and Beams* 17, 052801, 2014.

[27] P. Piot, A. Halavanau, D. Edstrom, J. Ruan, "A High-Level PYTHON Interface to ACNET", To appear in the proceedings of the North American Particle Accelerator Conference 2016 (NAPAC '16).

[28] P. Piot. Possible 1st-beam Lattice Setup(s) with One Cavity, *IOTA/ASTA Users Meeting*, Jan. 2015.

[29] `http://www.aps.anl.gov/Accelerator_Systems_Division/Accelerator_Operations_Physics/software.shtml`